



저작자표시-비영리-변경금지 2.0 대한민국

이용자는 아래의 조건을 따르는 경우에 한하여 자유롭게

- 이 저작물을 복제, 배포, 전송, 전시, 공연 및 방송할 수 있습니다.

다음과 같은 조건을 따라야 합니다:



저작자표시. 귀하는 원저작자를 표시하여야 합니다.



비영리. 귀하는 이 저작물을 영리 목적으로 이용할 수 없습니다.



변경금지. 귀하는 이 저작물을 개작, 변형 또는 가공할 수 없습니다.

- 귀하는, 이 저작물의 재이용이나 배포의 경우, 이 저작물에 적용된 이용허락조건을 명확하게 나타내어야 합니다.
- 저작권자로부터 별도의 허가를 받으면 이러한 조건들은 적용되지 않습니다.

저작권법에 따른 이용자의 권리는 위의 내용에 의하여 영향을 받지 않습니다.

이것은 [이용허락규약\(Legal Code\)](#)을 이해하기 쉽게 요약한 것입니다.

[Disclaimer](#)

이학박사 학위논문

**Enhanced Electrical Properties of  
Polythiophene-based Organic Field-Effect  
Transistors by Molecular Doping  
via Solid-State Diffusion**

고체상태 확산 분자도핑에 의한 폴리싸이오펜계  
유기 전계효과 트랜지스터의 전기적 특성 향상 연구

2020 년 2 월

서울대학교 대학원

물리·천문학부

김 영 록

# Enhanced Electrical Properties of Polythiophene-based Organic Field-Effect Transistors by Molecular Doping via Solid-State Diffusion



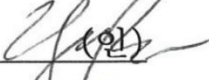

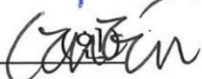
고체상태 확산 분자도핑에 의한 폴리싸이오펜계 유기 전계효과 트랜지스터의 전기적 특성 향상 연구

지도 교수 이 탁 희

이 논문을 이학박사 학위논문으로 제출함  
2020년 1월

서울대학교 대학원  
물리·천문학부 물리학 전공  
김 영 록

김영록의 이학박사 학위논문을 인준함  
2019년 12월

위원장	이진호	(인) 
부위원장	이탁희	(인) 
위원	박윤	(인) 
위원	양범정	(인) 
위원	임은주	(인) 

## **Abstract**

# **Enhanced Electrical Properties of Polythiophene-based Organic Field-Effect Transistors by Molecular Doping via Solid-State Diffusion**

**Youngrok Kim**

Department of Physics and Astronomy  
Seoul National University

Organic semiconductors (OSCs) have been widely studied due to their merits such as mechanical flexibility, solution processability, and large-area fabrication. Based on these merits, organic electronic devices, including organic light-emitting diodes, solar cells, sensors, memory and field effect transistors, have been widely investigated. In these organic electronic devices, downscaling and high-speed operation are essential for practical applications. However, a high contact resistance which arises from the Schottky contact between metal electrodes and OSCs fundamentally limits the device performance. In silicon-based semiconductor devices, selective ion implantation doping technique under the electrodes is widely used to enhance charge injection properties, and similar approach can be applied in OSCs to resolve the contact resistance issue. Recently, various contact doping methods have been reported as an effective way to reduce the contact resistance in organic electronic devices. However, the contact doping has not been explored extensively in organic field effect transistors (OFETs) due to the dopant diffusion problem which significantly degrades the device stability by damaging the ON/OFF switching performance.

In this thesis, firstly I demonstrated a selective contact doping of 2,3,5,6-tetrafluoro-

7,7,8,8-tetracyanoquinodimethane (F<sub>4</sub>-TCNQ) by solid-state diffusion in poly 2,5-bis(3-hexadecylthiophen-2-yl) thieno [3,2-b] thiophene (PBTTT) to enhance carrier injection properties in bottom-gate PBTTT OFETs. In this development, I investigated the effect of post-doping treatments on diffusion of F<sub>4</sub>-TCNQ molecules by using the experimental data and a numerical simulation based on a modified Fick's diffusion equation. Furthermore, the application of the doping technique to the low-voltage operation of PBTTT OFETs with high-k gate dielectrics demonstrated a potential for designing scalable and low-power organic devices by utilizing doping of conjugated polymers.

However, in spite of introducing post-doping treatments in order to confine the doped regions at the source-drain contact regions of OFETs, the dopant diffusion problem could not be resolved completely. Regarding this issue, I improved the stability of the contact doping method by selectively incorporating tetracyanoquinodimethane (TCNQ) as “dopant-blockade molecules” in PBTTT film in order to suppress the diffusion of the dopant molecules. The dopant-blockade molecules were carefully chosen such that they are electrically inactive and they readily locate themselves in the diffusion paths of the dopants within the active channel of the OFETs. This technique effectively constructed barriers against the motion of dopant molecules in the potential diffusion sites by filling them with the dopant-blockade molecules. Therefore, the dopant-blockade method will maximize the potential of OFETs by employing the contact doping method as a promising route towards resolving the contact resistance problem.

**Keywords:** Organic field effect transistors, dopant molecule, contact doping, solid-state diffusion, charge injection, charge transfer, dopant-blockade

**Student Number:** 2016-30095

# List of Contents

<b>Abstract .....</b>	<b>i</b>
<b>List of Contents.....</b>	<b>iii</b>
<b>List of Figures .....</b>	<b>v</b>
<b>Chapter 1. Introduction .....</b>	<b>1</b>
1.1. Brief introduction of organic electronics.....	1
1.2. Contact resistance problem in organic semiconductors .....	2
1.3. Contact doping via solid-state diffusion.....	3
1.4. Outline of this thesis.....	4
References .....	5

## **Chapter 2. Enhanced Charge Injection Properties of Organic**

### **Field Effect Transistor by Molecular Implantation**

<b>Doping .....</b>	<b>8</b>
2.1. Introduction .....	8
2.2. Experiments.....	11
2.2.1. Device fabrication process.....	11
2.2.2. Electrical characterization .....	15
2.2.3. Spectroscopy and microscopy .....	15
2.2.4. Contact resistance extraction by Y-function method .....	16
2.3. Results and discussions .....	18
2.3.1. Ultraviolet-visible absorption spectroscopy.....	18
2.3.2. Electrical characterization of PBTTT OFETs .....	19
2.3.3. ON/OFF ratio stability of the doped-contact PBTTT OFETs .....	21
2.3.4. Numerical simulation of the diffusion of F <sub>4</sub> -TCNQ .....	25

2.3.5. Band diagram analysis .....	30
2.3.6. Low-voltage operation OFETs by using high-k dielectric.....	33
2.4. Conclusion.....	37
References .....	38

## **Chapter 3. Highly stable contact doping in organic field effect**

### **transistors by dopant-blockade method .....43**

3.1. Introduction .....	43
3.2. Experiments.....	47
3.2.1. Materials and device fabrication process.....	47
3.2.2. Device and film characterization .....	51
3.3. Results and discussions .....	52
3.3.1. Ultraviolet-visible absorption spectroscopy.....	52
3.3.2. ToF-SIMS and XRR measurements.....	53
3.3.3. Electrical characterization of the DB/DC-FET .....	55
3.3.4. ON/OFF ratio stability of the DB/DC-FET .....	57
3.4. Conclusion.....	62
References .....	63

## **Chapter 4. Summary .....67**

### **국문초록(Abstract in Korean) .....69**

### **감사의 글 .....71**

# List of Figures

## Chapter 1.

**Figure 1.1** Examples of printing methods. (a) Ink-jet printing of OSCs. Reproduced from Ref.[17] (b) Demonstration of all-inkjet-printed organic inverter. Reproduced from Ref.[16] (c) Concept of gravure printing. Reproduced from Ref.[15] (d) Large-area processing by roll-to-roll gravure printing. Reproduced from Ref. [14]

## Chapter 2.

**Figure 2.1** (a) Schematic images of the device fabrication process. The dark green regions in the bottom-middle image represent neutral F<sub>4</sub>-TCNQ molecules and the bright green regions in the last two steps represent the doped PBTTT. (b) Molecular structures of PBTTT, F<sub>4</sub>-TCNQ, OTS. Adapted from Kim et al.

**Figure 2.2** A water droplet on (a) a pristine SiO<sub>2</sub> substrate and (b) an OTS SAM treated SiO<sub>2</sub> substrate. (c) AFM image of the PBTTT film deposited on the OTS SAM treated SiO<sub>2</sub> substrate. Adapted from Kim et al.

**Figure 2.3** Optical images of the selectively-doped PBTTT transistors. The black rectangular areas (right image) represent the doped regions of the PBTTT film. Adapted from Kim et al.

**Figure 2.4** (a) TEM cross-section image of the etched PBTTT film. (b) Oxygen element signals. (c) Sulfur element signals. (d) Argon element signals. (e) Carbon element signals. (f) Silicon element signals. Adapted from Kim et al.

**Figure 2.5** (a) AFM image of the etched PBTTT film. (b) AFM image of the doped and unetched PBTTT film. (c) AFM image of the doped and etched PBTTT film. Adapted from Kim et al.

**Figure 2.6** UV-Vis spectra for pristine PBTTT, etched PBTTT, doped/unetched PBTTT, and doped/etched PBTTT films. The shaded area (in green) denotes a broad polaron absorption. Adapted from Kim et al.

**Figure 2.7**  $I_{DS}-V_{GS}$  transfer curves of (a) the pristine and (b) doped contact (doped/etched) PBTTT transistor. (c)  $I_{DS}-V_{DS}$  output curves of a doped contact (doped/etched) PBTTT



transistor. Adapted from Kim et al.

**Figure 2.8**  $I_{DS}$ - $V_{GS}$  transfer curves of the pristine PBTTT transistor (a) before etching and (b) after etching. Adapted from Kim et al.

**Figure 2.9** (a) A water droplet on a pristine PBTTT film. (b) A water droplet on an etched PBTTT film. Adapted from Kim et al.

**Figure 2.10**  $I_{DS}$ - $V_{GS}$  transfer curves, Y-function and  $1/\sqrt{g_m}$  plotted with  $V_{GS}$  for (a) the pristine PBTTT transistor and (b) the doped contact PBTTT transistor. Adapted from Kim et al.

**Figure 2.11** The time evolution of transfer curves for (a) the doped/unetched PBTTT transistor with the channel length,  $L_{ch}$ , of 50  $\mu\text{m}$ , (b) the doped/unetched PBTTT transistor with  $L_{ch} = 100 \mu\text{m}$ , (c) the doped contact (doped/etched) PBTTT transistor with  $L_{ch} = 50 \mu\text{m}$ , and (d) the doped contact PBTTT transistor with  $L_{ch} = 100 \mu\text{m}$  for two months. (e) ON/OFF ratio stability for the doped PBTTT transistors with a channel length ( $L$ ) of 50  $\mu\text{m}$  and 100  $\mu\text{m}$ . (f) Schematic images of doped region propagation by the neutral dopants diffusion. Adapted from Kim et al.

**Figure 2.12**  $I_{DS}$ - $V_{GS}$  transfer curves of (a) the CYTOP encapsulated doped contact PBTTT transistor with the channel length of 50  $\mu\text{m}$  and (b) the CYTOP encapsulated doped contact PBTTT transistor with the channel length of 100  $\mu\text{m}$  for more than two months. (c) The ON/OFF ratio stability for the doped contact and CYTOP encapsulated doped contact transistors. Adapted from Kim et al.

**Figure 2.13** Optical images of the rectangular doped regions with the 50  $\mu\text{m}$  gap in the (a) doped/unetched and (b) doped/etched PBTTT film for one week. Adapted from Kim et al.

**Figure 2.14** (a) The evolution of the neutral dopant concentration of the doped/unetched device. (b) The evolution of the doping fraction of the PBTTT molecules of the doped/unetched device. (c) The evolution of the neutral dopant concentration of the doped/etched device. (d) The evolution of the doping fraction of the PBTTT molecules of the doped/etched device. Adapted from Kim et al.

**Figure 2.15** (a)  $I_{DS}$ - $V_{DS}$  output curves of an entire-doped PBTTT device at  $V_{GS} = 0 \text{ V}$  in a temperature range from 80 K to 300 K. (b)  $\ln(I_{DS}/T^{3/2})$  vs  $1/T$  at  $V_{GS} = 0 \text{ V}$ . (c)  $\ln(I_{DS}/T^{3/2})$  vs  $1/T$  at  $V_{GS} = -20 \text{ V}$ . (d)  $\ln(I_{DS}/T^{3/2})$  vs  $1/T$  at  $V_{GS} = -40 \text{ V}$ . (e)  $\ln(I_{DS}/T^{3/2})$  vs  $1/T$  at  $V_{GS} = -60 \text{ V}$ . (f) The plots of activation energies vs  $V_{DS}$ . Adapted from Kim et al.

**Figure 2.16** (a) The UPS data of 50 nm-thick Au films near the Fermi level and secondary-

electron cut-off. (b) The UPS data of the doped/unetched and pristine PBTTT films near the Fermi level (right) and secondary-electron cut-off (left). Adapted from Kim et al.

**Figure 2.17** The band diagram near the contact of (a) the pristine PBTTT transistor and (b) the doped contact PBTTT transistor, with a highlighted view of the band diagram at the contact. Adapted from Kim et al.

**Figure 2.18** The fabrication process of the high-k PBTTT transistors on Al<sub>2</sub>O<sub>3</sub>. Adapted from Kim et al.

**Figure 2.19** The measured capacitance data of the deposited Al<sub>2</sub>O<sub>3</sub>. The calculated capacitance value of 270 nm SiO<sub>2</sub> is displayed in below for comparison. Adapted from Kim et al.

**Figure 2.20** (a) A water droplet on a pristine Al<sub>2</sub>O<sub>3</sub> substrate. (b) A water droplet on the OTS SAM treated Al<sub>2</sub>O<sub>3</sub> substrate. (c) AFM image of the PBTTT film deposited on the OTS SAM treated Al<sub>2</sub>O<sub>3</sub> substrate. Adapted from Kim et al.

**Figure 2.21** (a) The  $I_{DS}-V_{GS}$  transfer curve of the doped contact transistor and (b) the pristine transistor with OTS SAM treated Al<sub>2</sub>O<sub>3</sub>. The black lines represent the gate leakage current in the devices. Adapted from Kim et al.

**Figure 2.22** (a)  $I_{DS}-V_{GS}$  transfer curves of the doped contact and pristine PBTTT transistors. Linear plots of the output curves are shown in the inset. (b)  $I_{DS}-V_{DS}$  output curves of the doped contact and pristine PBTTT transistors. Adapted from Kim et al.

### Chapter 3.

**Figure 3.1** (a) Molecular structures of PBTTT, F<sub>4</sub>-TCNQ, TCNQ and OTS. (b) HOMO and LUMO levels of PBTTT and F<sub>4</sub>-TCNQ. (c) HOMO and LUMO levels of PBTTT and TCNQ. Adapted from Kim et al.

**Figure 3.2** Schematic images of (a) the PBTTT OFET and (b) the PBTTT OFET with TCNQ molecules deposited on the entire PBTTT channel. (c) The transfer curves of the PBTTT OFET (black line) and PBTTT OFET with TCNQ molecules deposited on the entire PBTTT channel (red line). Adapted from Kim et al.

**Figure 3.3** Schematic images of the fabrication process of the dopant-blockade PBTTT OFET. The red regions in the middle of transistors is the TCNQ-incorporated regions. The dark green regions represent the neutral F<sub>4</sub>-TCNQ molecules which are not involved

in the charge transfer reaction with PBTTT molecules. The bright green regions are the doped-PBTTT regions by using F<sub>4</sub>-TCNQ dopant molecules. Adapted from Kim et al.

**Figure 3.4** The surface morphology of the PBTTT film deposited on the OTS-treated SiO<sub>2</sub>/Si substrate measured by atomic force microscope. Adapted from Kim et al.

**Figure 3.5** UV-Vis spectroscopy data for the pristine PBTTT film (black line), PBTTT/TCNQ film (red line) and PBTTT/F<sub>4</sub>-TCNQ film. Adapted from Kim et al.

**Figure 3.6** (a) The depth profiles of ion intensity for the pristine PBTTT film (dashed lines and empty symbols) and PBTTT/TCNQ film (solid lines and filled symbols); the sulfur ion signals are black solid and dashed lines, the oxygen ion blue solid and dashed lines, silicon ion green solid and dashed lines and the cyanide ion signal red empty and filled circle symbols. (b) The XRR data of the pristine PBTTT film (black line), the PBTTT/TCNQ film (red line) and the PBTTT/F<sub>4</sub>-TCNQ film (green line). The intervals between large  $q_z$  peaks of each film represent the out-of-plane lamellar stacking distance. Adapted from Kim et al.

**Figure 3.7** (a) Schematic images of the DC-FET (w/o TCNQ) and DB/DC-FET (with TCNQ). The transfer curves of (b) the DC-FET and (c) the DB/DC-FET. (d) The output curves of the DB/DC-FET. Adapted from Kim et al.

**Figure 3.8** Data for Y-function method; a black line shows  $1/\sqrt{g_m}$  (where  $g_m$  is the transconductance), a red line is the Y-function and a blue dashed line represents the selected data to extract contact resistance. Adapted from Kim et al.

**Figure 3.9** Time evolution of the transfer curves for (a) the DC-FET with the channel length,  $L_{ch}$ , of 50  $\mu\text{m}$ , (b) the DB/DC-FET with  $L_{ch} = 50 \mu\text{m}$ , (c) the DC-FET with  $L_{ch} = 100 \mu\text{m}$  and (d) the DB/DC-FET with  $L_{ch} = 100 \mu\text{m}$  over two months. (e) The ON/OFF ratio of the DC-FET and the DB/DC-FET over time with the channel length of 50  $\mu\text{m}$  and 100  $\mu\text{m}$ . Adapted from Kim et al.

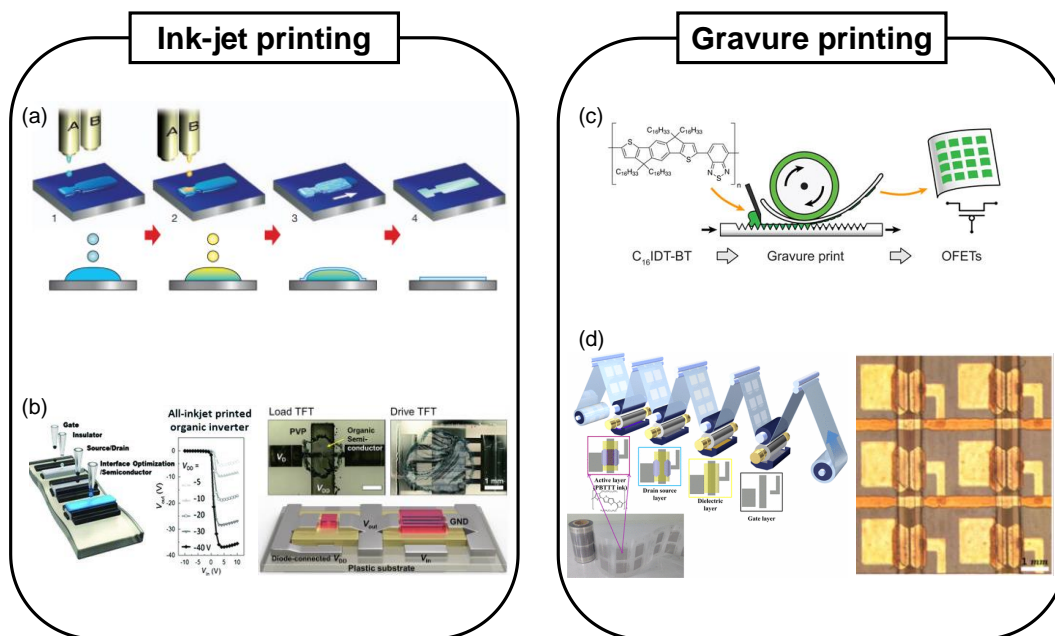
**Figure 3.10** Schematic diagrams of (a) the propagation of doped regions in the DC-FET, (b) the diffusion of TCNQ molecules in the channel region of the TCNQ-incorporated PBTTT OFET and (c) the diffusion of F<sub>4</sub>-TCNQ and TCNQ molecules in the opposite directions for the DB/DC-FET. (d) The illustration for hindrance by the dopant-blockade molecules against the diffusion of the dopant molecules in the void spaces of the PBTTT film. (e) The predicted profiles of the doped fraction of PBTTT molecules at different positions of the channel in the DC-FET. (f) The spatial diffusion profile of TCNQ

molecules in the PBTTT channel of the TCNQ-incorporated PBTTT OFET. (g) The predicted changes in the profiles of the doped fraction of PBTTT molecules and the spatial diffusion of TCNQ molecules for the DB/DC-FET as blue and red solid lines. Dashed lines taken from Figure 3.10e and f for comparison. Adapted from Kim et al.

# Chapter 1. Introduction

## 1.1. Brief introduction of organic electronics

The advantages of these organic semiconductors (OSCs) include mechanical flexibility, solution processability, and tunable material functionalities by molecular-design.<sup>[1-13]</sup> Based on these advantages, organic electronic devices, including organic light-emitting diodes (OLED), solar cells, sensors, memory and organic field effect transistors (OFETs), have been widely investigated. Solution processability and mechanical flexibility could lead to printing fabrication process. There have been two major printing methods; inkjet and roll-to-roll gravure printing.<sup>[14-17]</sup> In the ink-jet printing method, the electronic devices have made by an ink-jet printer which uses semiconducting and conducting inks as



**Figure 1.1** Examples of printing methods. (a) Ink-jet printing of OSCs. Reproduced from Ref.[17] (b) Demonstration of all-inkjet-printed organic inverter. Reproduced from Ref.[16] (c) Concept of gravure printing. Reproduced from Ref.[15] (d) Large-area processing by roll-to-roll gravure printing. Reproduced from Ref. [14]

shown in Figure 1.1a and 1.1b.<sup>[16,17]</sup> By the ink-jet printing method, the organic electronic device with complex structure could be fabricated at low temperature. On the other hand, in the gravure printing method, electronic circuits have been drawn as a newspaper as shown in the figure 1.1c and d on flexible substrates which are introduced between rolls.<sup>[14,15]</sup> Electronic circuits could be produced in large areas with high throughput at low temperature by gravure printing method.

The advantage of tunable material functionalities have been suitable properties for optoelectronic device application. Relying on this advantage, organic solar cells have been extensively studied and, recently, the organic solar cell which recorded more than 16% efficiency has been reported.<sup>[18-24]</sup> But above all, this advantage of OSCs has been especially evident in OLEDs.<sup>[25-32]</sup> By controlling the optoelectric properties of OSCs, high level of color reproduction could be realized, and OLED display is now fully commercialized.

## **1.2. Contact resistance problem in organic semiconductors**

If it is possible advancing the performance of OFETs to keep pace with the industrial success of OLEDs, OFETs could be potentially applied as switching and driving transistors in demonstrating the fully-flexible organic display panels.<sup>[33,34]</sup> In this application, to meet technological demands of display panels, the development of downscaling and high-speed operation of OFETs has been an essential bottleneck. However, the contact resistance problem arising between OSCs and metal electrodes has been one of the dominant obstacles for using OFETs because the high contact resistance which increases the operation voltage of transistors fundamentally limits the device performance of OFET as a switching transistor.<sup>[35-37]</sup> To overcome this problem, there have been various

approaches, including self-assembled monolayer treatment on electrodes and introducing charge injection layers.<sup>[38-44]</sup> At the start, I looked at how the established silicon metal-oxide-semiconductor field-effect transistor (MOSFET) technology solved this problem. In MOSFET fabrication, the contact doping by ion implantation technique has been widely used before the metal electrode deposition. This technique decreases the contact resistance by reducing the carrier depletion width at the interface between metal electrodes and semiconductors. Today, for silicon MOSFET industry, ion implantation doping technique has become an essential process in the fabrication of an integrated circuit.

### **1.3. Contact doping via solid-state diffusion**

For introducing the dopant implantation technique in OCSs, I needed to find a proper material combination enabling a high carrier concentration, high conductivity, and controllability similar to silicon-boron and silicon-phosphorus combinations. Recently, solid-state diffusion phenomenon and its physical properties was reported with the combination of PBTTT and F<sub>4</sub>-TCNQ; PBTTT as an organic semiconductor and F<sub>4</sub>-TCNQ as a dopant molecule.<sup>[45]</sup> This materials combination exhibited various advantages in application for organic transistors; a high conductivity up to 200 S/cm, high carrier concentration up to  $3.3 \times 10^{20} \text{ cm}^{-3}$  and doped-region controllability. Therefore, this combination was a strong candidate to utilize the contact-doping technique for resolving the contact resistance issue in OFETs. For implementing the contact-doping technique, one of the most difficult challenges has lied in confining the doped regions away from the channel regions of OFETs (i.e. in localized regions at the source-drain contacts only). The diffusion problem usually leads to undesirable degradation in the switching performance of devices, and therefore the device stability reduces over time.<sup>[46,47]</sup> To resolve the dopant

diffusion problem in the contact-doping technique, three kinds of approaches were developed in this thesis; the surface etching treatment, incorporation of a passivation layer and the “dopant-blockade” method.

## **1.4. Outline of this thesis**

This thesis mainly focuses on the electrical properties and operational stability of the doped-contact PBTTT OFETs. In chapter 2, I discuss the development of the contact-doping technique via solid-state diffusion and the analysis of the device properties of the doped-contact PBTTT OFETs by experimental data and numerical simulation. In chapter 3, I suggest the incorporation of dopant-blockade molecules which could not change the electrical properties of PBTTT OFETs to enhance the device stability by suppressing the dopant diffusion. Finally, chapter 4 summaries this study.



## References

- [1] X. Gu, L. Shaw, K. Gu, M. F. Toney, Z. Bao, *Nat. Commun.* **2018**, 9, 534.
- [2] W.-Y. Lee, H.-C. Wu, C. Lu, B. D. Naab, W.-C. Chen, Z. Bao, *Adv. Mater.* **2017**, 29, 1605166.
- [3] T. Someya, Z. Bao, G. G. Malliaras, *Nature* **2016**, 540, 379.
- [4] H. Sirringhaus, *Adv. Mater.* **2014**, 26, 1319.
- [5] M. Kaltenbrunner, T. Sekitani, J. Reeder, T. Yokota, K. Kuribara, T. Tokuhara, M. Drack, R. Schwödianer, I. Graz, S. Bauer-Gogonea, S. Bauer, T. Someya, *Nature* **2013**, 499, 458.
- [6] H. Kang, R. Kitsomboonloha, J. Jang, V. Subramanian, *Adv. Mater.* **2012**, 24, 3065.
- [7] T. Sekitani, T. Someya, *Mater. Today* **2011**, 14, 398.
- [8] A. de la Fuente Vornbrock, D. Sung, H. Kang, R. Kitsomboonloha, V. Subramanian, *Org. Electron.* **2010**, 11, 2037.
- [9] T. Sekitani, H. Nakajima, H. Maeda, T. Fukushima, T. Aida, K. Hata, T. Someya, *Nat. Mater.* **2009**, 8, 494.
- [10] T. Sekitani, M. Takamiya, Y. Noguchi, S. Nakano, Y. Kato, T. Sakurai, T. Someya, *Nat. Mater.* **2007**, 6, 413.
- [11] Y.-Y. Noh, N. Zhao, M. Caironi, H. Sirringhaus, *Nat. Nanotechnol.* **2007**, 2, 784.
- [12] J. B. Lee, V. Subramanian, *IEEE Trans. Electron Devices* **2005**, 52, 269.
- [13] G. Yu, J. Gao, J. C. Hummelen, F. Wudl, A. J. Heeger, *Science* **1995**, 270, 1789.
- [14] J. Sun, H. Park, Y. Jung, G. Rajbhandari, B. B. Maskey, A. Sapkota, Y. Azuma, Y. Majima, G. Cho, *ACS Omega* **2017**, 2, 5766.
- [15] S. G. Higgins, B. V. O. Muir, M. Heeney, A. J. Campbell, *MRS Commun.* **2015**, 5, 599.
- [16] S. Chung, M. Jang, S.-B. Ji, H. Im, N. Seong, J. Ha, S.-K. Kwon, Y.-H. Kim, H. Yang, Y. Hong, *Adv. Mater.* **2013**, 25, 4773.
- [17] H. Minemawari, T. Yamada, H. Matsui, J. Tsutsumi, S. Haas, R. Chiba, R. Kumai, T. Hasegawa, *Nature* **2011**, 475, 364.
- [18] Y. Cui, H. Yao, J. Zhang, T. Zhang, Y. Wang, L. Hong, K. Xian, B. Xu, S. Zhang, J. Peng, Z. Wei, F. Gao, J. Hou, *Nat. Commun.* **2019**, 10, 2515.
- [19] D.-H. Kim, T.-M. Kim, W.-I. Jeong, J.-J. Kim, *Appl. Phys. Lett.* **2012**, 101, 153303.

- [20] Y.-H. Chen, L.-Y. Lin, C.-W. Lu, F. Lin, Z.-Y. Huang, H.-W. Lin, P.-H. Wang, Y.-H. Liu, K.-T. Wong, J. Wen, D. J. Miller, S. B. Darling, *J. Am. Chem. Soc.* **2012**, 134, 13616.
- [21] G. Garcia-Belmonte, J. Bisquert, *Appl. Phys. Lett.* **2010**, 96, 113301.
- [22] D. Cheyuns, B. P. Rand, P. Heremans, *Appl. Phys. Lett.* **2010**, 97, 033301.
- [23] B. P. Rand, D. P. Burk, S. R. Forrest, *Phys. Rev. B* **2007**, 75, 115327.
- [24] M. C. Scharber, D. Mühlbacher, M. Koppe, P. Denk, C. Waldauf, A. J. Heeger, C. J. Brabec, *Adv. Mater.* **2006**, 18, 789.
- [25] K.-H. Kim, S. Lee, C.-K. Moon, S.-Y. Kim, Y.-S. Park, J.-H. Lee, J. W. Lee, J. Huh, Y. You, J.-J. Kim, *Nat. Commun.* **2014**, 5, 4769.
- [26] Y.-S. Park, S. Lee, K.-H. Kim, S.-Y. Kim, J.-H. Lee, J.-J. Kim, *Adv. Funct. Mater.* **2013**, 23, 4914.
- [27] K. Goushi, K. Yoshida, K. Sato, C. Adachi, *Nat. Photonics* **2012**, 6, 253.
- [28] M. G. Helander, Z. B. Wang, J. Qiu, M. T. Greiner, D. P. Puzzo, Z. W. Liu, Z. H. Lu, *Science* **2011**, 332, 944.
- [29] S. Hamwi, J. Meyer, M. Kröger, T. Winkler, M. Witte, T. Riedl, A. Kahn, W. Kowalsky, *Adv. Funct. Mater.* **2010**, 20, 1762.
- [30] M. A. Baldo, S. Lamansky, P. E. Burrows, M. E. Thompson, S. R. Forrest, *Appl. Phys. Lett.* **1999**, 75, 4.
- [31] M. A. Baldo, D. F. O'brien, Y. You, A. Shoustikov, S. Sibley, M. E. Thompson, S. R. Forrest, *Nature* **1998**, 395, 151.
- [32] C. W. Tang, S. A. VanSlyke, C. H. Chen, *J. Appl. Phys.* **1989**, 65, 3610.
- [33] T. Sekitani, T. Someya, *MRS Bull.* **2012**, 37, 236.
- [34] L. Zhou, A. Wanga, S.-C. Wu, J. Sun, S. Park, T. N. Jackson, *Appl. Phys. Lett.* **2006**, 88, 083502.
- [35] A. Perinot, P. Kshirsagar, M. A. Malvindi, P. P. Pompa, R. Fiammengo, M. Caironi, *Sci. Rep.* **2016**, 6, 38941.
- [36] T. Uemura, T. Matsumoto, K. Miyake, M. Uno, S. Ohnishi, T. Kato, M. Katayama, S. Shinamura, M. Hamada, M.-J. Kang, K. Takimiya, C. Mitsui, T. Okamoto, J. Takeya, *Adv. Mater.* **2014**, 26, 2983.
- [37] F. Ante, D. Kälblein, T. Zaki, U. Zschieschang, K. Takimiya, M. Ikeda, T. Sekitani, T. Someya, J. N. Burghartz, K. Kern, H. Klauk, *Small* **2012**, 8, 73.

- [38] D. He, J. Qiao, L. Zhang, J. Wang, T. Lan, J. Qian, Y. Li, Y. Shi, Y. Chai, W. Lan, L. K. Ono, Y. Qi, J.-B. Xu, W. Ji, X. Wang, *Sci. Adv.* **2017**, 3, e1701186.
- [39] C. G. Tang, M. C. Y. Ang, K.-K. Choo, V. Keerthi, J.-K. Tan, M. N. Syafiqah, T. Kugler, J. H. Burroughes, R.-Q. Png, L.-L. Chua, P. K. H. Ho, *Nature* **2016**, 539, 536.
- [40] J. Youn, G. R. Dholakia, H. Huang, J. W. Hennek, A. Facchetti, T. J. Marks, *Adv. Funct. Mater.* **2012**, 22, 1856.
- [41] T. Minari, P. Darmawan, C. Liu, Y. Li, Y. Xu, K. Tsukagoshi, *Appl. Phys. Lett.* **2012**, 100, 093303.
- [42] K. A. Singh, T. L. Nelson, J. A. Belot, T. M. Young, N. R. Dhumal, T. Kowalewski, R. D. McCullough, P. Nachimuthu, S. Thevuthasan, L. M. Porter, *ACS Appl. Mater. Interfaces* **2011**, 3, 2973.
- [43] Y.-Y. Noh, X. Cheng, M. Tello, M.-J. Lee, H. Sirringhaus, *Semicond. Sci. Technol.* **2011**, 26, 034003.
- [44] F. Gholamrezaie, K. Asadi, R. A. H. J. Kicken, B. M. W. Langeveld-Voss, D. M. de Leeuw, P. W. M. Blom, *Synth. Met.* **2011**, 161, 2226.
- [45] K. Kang, S. Watanabe, K. Broch, A. Sepe, A. Brown, I. Nasrallah, M. Nikolka, Z. Fei, M. Heeney, D. Matsumoto, K. Marumoto, H. Tanaka, S.-i. Kuroda, H. Sirringhaus, *Nat. Mater.* **2016**, 15, 896.
- [46] Y. Kim, S. Chung, K. Cho, D. Harkin, W.-T. Hwang, D. Yoo, J.-K. Kim, W. Lee, Y. Song, H. Ahn, Y. Hong, H. Sirringhaus, K. Kang, T. Lee, *Adv. Mater.* **2019**, 31, 1806697.
- [47] Y. Xu, H. Sun, E.-Y. Shin, Y.-F. Lin, W. Li, Y.-Y. Noh, *Adv. Mater.* **2016**, 28, 8531.

# Chapter 2. Enhanced Charge Injection Properties of Organic Field Effect Transistor by Molecular Implantation

## Doping

*Organic semiconductors (OSCs) have been widely studied due to their merits such as mechanical flexibility, solution processability, and large-area fabrication. However, OSCs devices still have to overcome contact resistance issues for better performances. To improve the contact properties of OSCs, there have been several methods reported, including interface treatment by self-assembled monolayers and introducing charge injection layers. However, because of the Schottky contact at the metal-OSC interfaces, a non-ideal transfer curve feature often appears in the low drain voltage region. Here, I demonstrated a selective contact doping of 2,3,5,6-tetrafluoro-7,7,8,8-tetracyanoquinodimethane ( $F_4$ -TCNQ) by solid-state diffusion in poly 2,5-bis(3-hexadecylthiophen-2-yl) thieno [3,2-b] thiophene (PBTTT) to enhance carrier injection in bottom-gate PBTTT organic field effect transistors (OFETs). Furthermore, I have investigated the effect of post-doping treatment on diffusion of  $F_4$ -TCNQ molecules in order to improve the device stability. In addition, the application of the doping technique to the low-voltage operation of PBTTT OFETs with high-k gate dielectrics demonstrated a potential for designing scalable and low-power organic devices by utilizing doping of conjugated polymers.*

### 2.1. Introduction

Organic semiconductors (OSCs), widely applied as electronic devices such as organic light-emitting diodes, solar cells, memories and organic field effect transistors (OFETs), have various advantages including mechanical flexibility, low-cost, solution-processed fabrication and tunable material functionalities by molecular-design compared to silicon-based materials.<sup>[1-13]</sup> However, the contact resistance problem arising between

organic materials and metal electrodes has been one of the dominant obstacles for adopting organic semiconducting devices instead of silicon-based devices. Diverse attempts, for instance, self-assembled monolayer (SAM) treatment on metal electrodes,<sup>[14-19]</sup> inserting a charge injection layer between organic semiconductor and metals,<sup>[20-27]</sup> choice of metals for better injection properties,<sup>[28-29]</sup> adopting carbon-based conductor like graphene as electrodes,<sup>[30]</sup> have been introduced to improve carrier injection across typically a non-ohmic contact. Especially, considering large operation voltages required for OFETs, improving contact properties of organic/metal interface is an essential step for practical applications of OSCs.

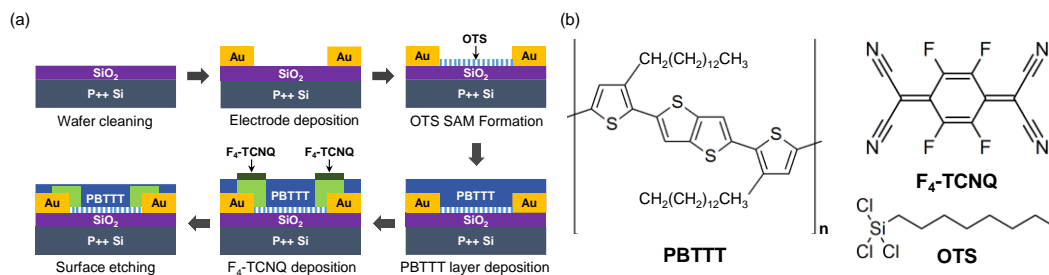
Contact doping is one of the most effective technique to reduce contact resistance and has been widely employed in silicon-based devices and recently in OSCs to reduce the contact resistance.<sup>[31-36]</sup> In order to avoid undesirable OFF currents it needs to be performed selectively, i.e., in localized regions at the source-drain contacts only and not in the channel region. The doped regions have been usually confined to the top surface of the organic semiconductor film by depositing a small amount of dopants on the top of the organic film by thermal evaporation. As a result, the position of the gate dielectrics was normally restricted to the top side of devices (i.e. FETs in a top-gate structure) in order to enhance the charge injection from metal electrodes to the accumulation layer formed on the top surface of the polymer.<sup>[31-32]</sup> Recently, the combination of poly(2,5-bis(3-tetradecylthiophen-2-yl)thieno[3,2-b]thiophene) (PBTTT) and 2,3,5,6-tetrafluoro-7,7,8,8-tetracyanoquinodimethane (F<sub>4</sub>-TCNQ) as host and dopant material, respectively, has produced a highly conducting polymer that has been studied as a candidate for a synthetic metal and high power-factor thermoelectric material.<sup>[37-41]</sup> Interestingly, this combination achieved an efficient bulk-doping of PBTTT by solid-state diffusion which implied that the

F<sub>4</sub>-TCNQ dopant molecules diffused into the PBTTT film all the way down to the interface between the PBTTT film and the SiO<sub>2</sub>/Si substrate.<sup>[39]</sup> Moreover, the PBTTT film doped by solid-state diffusion exhibits a high conductivity of around 200 S/cm which would be applicable for selective contact doping for FETs.

One of the main challenges in utilizing selective molecular doping in organic optoelectronic devices has been the diffusion problem of dopant molecules in the host materials, which has reduced the device stability.<sup>[42-47]</sup> The dopant diffusion will especially be significant if one adopts selective bulk-doping on the contact regions of OFETs due to a large dopant concentration gradient of dopant molecules between the doped regions and active channel (non-doped) regions. To this date, there has been a relatively small number of studies that have directly investigated the diffusion problems within the selectively contact-doped OFETs.<sup>[32]</sup> In this chapter, the bulk-doping technique of PBTTT by solid-state diffusion of F<sub>4</sub>-TCNQ was employed to provide highly conducting paths in order to enhance the charge injection in PBTTT OFETs in a bottom-gate structure. This technique is akin to an ion implantation doping technique employed in the silicon industry; hence the name, “molecular implantation doping”. I investigated and further improved the stability of the PBTTT OFETs by characterizing the effect of post-doping treatments on the dopant diffusion into the active channel. Moreover, I demonstrated that introducing the molecular implantation doping technique to the PBTTT OFETs with high-k gate dielectrics enabled a low-voltage operation, with improved charge injection properties.

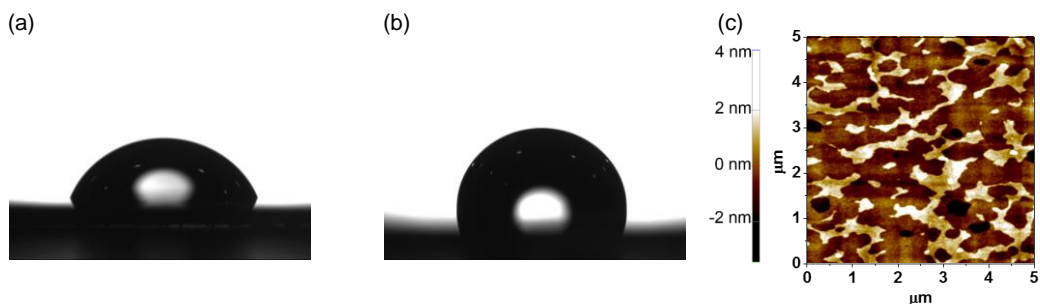
## 2.2. Experiments

### 2.2.1. Device fabrication process



**Figure 2.1** (a) Schematic images of the device fabrication process. The dark green regions in the bottom-middle image represent neutral F<sub>4</sub>-TCNQ molecules and the bright green regions in the last two steps represent the doped PBTTT. (b) Molecular structures of PBTTT, F<sub>4</sub>-TCNQ, OTS.

Figure 2.1a and b show the fabrication process of PBTTT OFETs with F<sub>4</sub>-TCNQ doping on the contact regions of the devices and molecular structures of the used materials, respectively. SiO<sub>2</sub>/Si substrates were cleaned using de-ionized water, isopropanol and acetone for 10 min in each cleaning solvent by sonication in an ultrasonic bath. Then, the electrodes consisting of Au (30 nm-thick)/Ti (2 nm-thick) were deposited with shadow masks on the substrates by using an electron-beam evaporator with a deposition rate of 0.5 Å/s at a pressure of  $\sim 10^{-7}$  torr. After further cleaning with an oxygen plasma etching (50 W for 2 min) to optimize the surface properties, the substrates were transferred immediately to a nitrogen atmosphere glove box and were immersed in a prepared octyltrichlorosilane (OTS, Sigma-Aldrich) solution (30 mM in anhydrous toluene (Sigma-Aldrich)) for  $\sim 12$  hours to form the saturated coverage of OTS self-assembled monolayers (SAMs) on the SiO<sub>2</sub> surfaces.<sup>[48]</sup> At the end of the OTS SAM treatment, the substrates were transferred out from the glove box while being immersed in anhydrous toluene. The substrates were cleaned in toluene, isopropanol, acetone and toluene again by sonication for 10 min in each

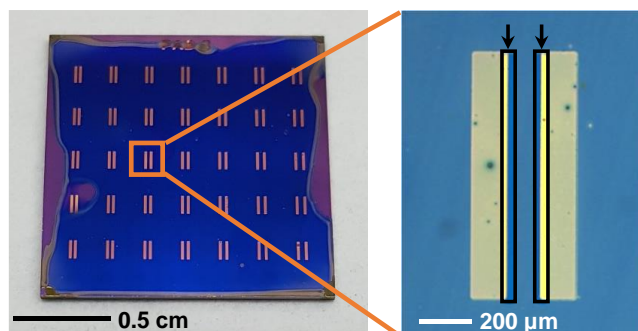


**Figure 2.2** A water droplet on (a) a pristine SiO<sub>2</sub> substrate and (b) an OTS SAM treated SiO<sub>2</sub> substrate. (c) AFM image of the PBTTT film deposited on the OTS SAM treated SiO<sub>2</sub> substrate.

solvent to remove residual OTS molecules on the SiO<sub>2</sub> surfaces. To evaporate the residual cleaning solvents, the substrates were stocked in a vacuum chamber for ~2 hours. Figure 2.2a and b show the water droplets on both the pristine and OTS SAM treated SiO<sub>2</sub> substrates. The measured contact angle was changed from 65.4° to 97.9° after the OTS SAM treatment.<sup>[48]</sup> The polymer semiconductor solution was prepared as poly[2,5-bis(3-tetradecylthiophen-2-yl)thieno[3,2-*b*]thiophene] (PBTTT, Sigma-Aldrich) in anhydrous 1,2-dichlorobenzene (DCB, Sigma-Aldrich) solution (9 mg mL<sup>-1</sup>). Before spin-coating, the PBTTT solution was heated at 110 °C to form uniform PBTTT films. The PBTTT films were spin-coated at 1500 rpm for 45 s in the N<sub>2</sub>-filled glove box, followed by annealing at 180 °C for 20 min, and then the films were cooled down to room temperature slowly. Figure 2.2c shows the atomic force microscopy (AFM) image of the PBTTT films deposited on the OTS SAM treated SiO<sub>2</sub>, displaying clear terrace structures with 2 nm steps.<sup>[48-51]</sup>

Then, the dopant material, F<sub>4</sub>-TCNQ, was thermally evaporated directly onto the selected region of PBTTT layer with a nominal thickness of 10 nm by shadow masks with a deposition rate of 0.5–1.5 Å/s at a pressure of ~10<sup>-6</sup> torr as depicted in Figure 2.1a. The dopant molecules diffuse into the PBTTT film, creating a decaying depth-profile of the dopant distribution.<sup>[39]</sup> Therefore, it was crucial to optimize the amount of dopants so that I

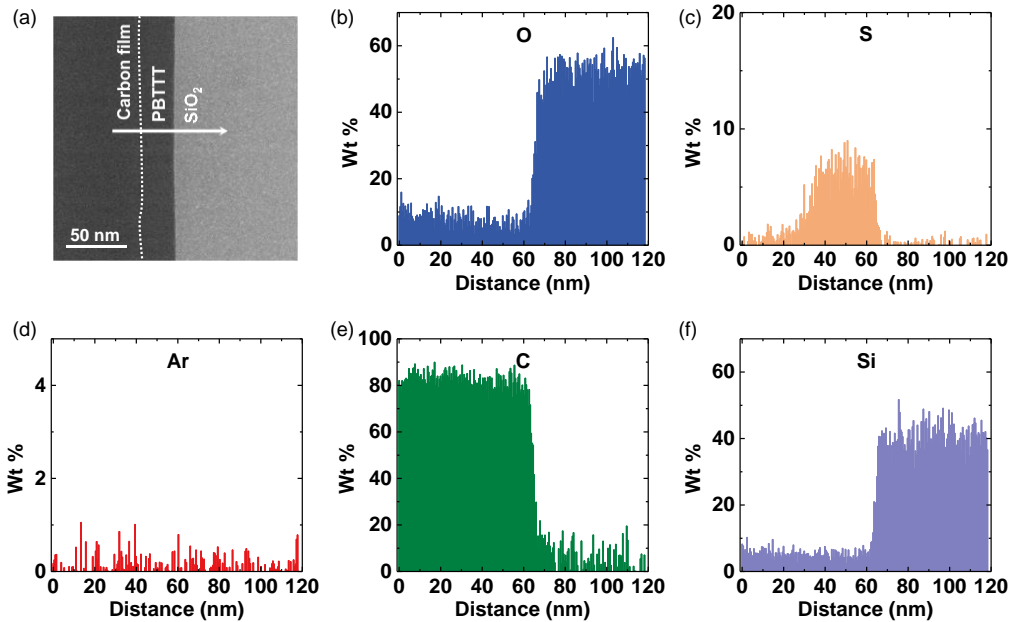




**Figure 2.3** Optical images of the selectively-doped PBTTT transistors. The black rectangular areas (right image) represent the doped regions of the PBTTT film.

can still achieve a good conductivity at the regions near the contact electrodes to enhance charge injection, while suppressing the dopant diffusion near the top surface. The doped regions of the PBTTT film appear more transparent as shown in the marked regions with arrows in the right image of Figure 2.3.

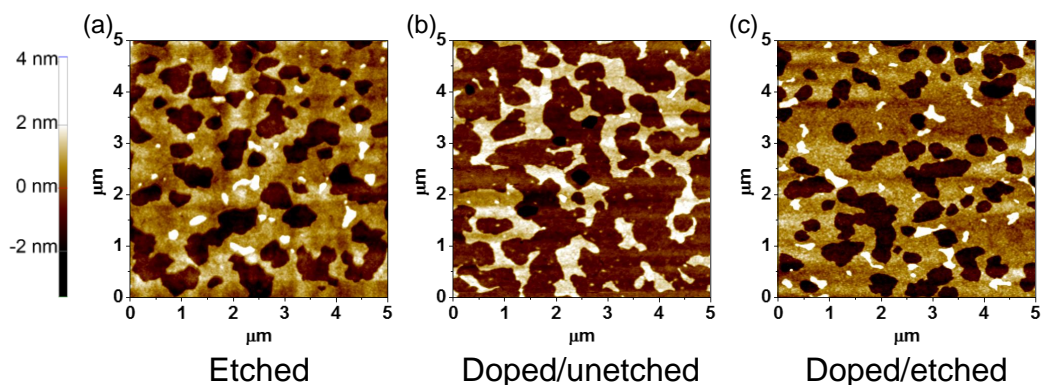
When the dopant deposition was finished, the surface of the PBTTT films were immediately by argon plasma etching (50 W for 1 s) to minimize diffusion of the dopant which caused a rise of the off-current of the OFET (defined as the minimum current value during the gate bias sweeps). The etching process was done because I anticipated the diffusion of the dopant into the channel to be mainly caused by the neutral dopant molecules which did not undergo charge transfer with PBTTT. It was suggested from the previous research that the etching rate of F<sub>4</sub>-TCNQ molecules was much faster than that of PBTTT and the neutral dopant molecules mainly remained near the surface of the PBTTT film.<sup>[39]</sup> Therefore, I inferred that the etching process reduced the neutral dopant concentration near the top surface of the doped regions of the PBTTT films. From the transmission electron microscopy (TEM) cross-section image and energy dispersive spectrometer (EDS) element analysis, I found that the thickness of the PBTTT film was ~30 nm by tracing the sulfur signals. Figure 2.4 shows a transmission electron microscopy



**Figure 2.4** (a) TEM cross-section image of the etched PBTTT film. (b) Oxygen element signals. (c) Sulfur element signals. (d) Argon element signals. (e) Carbon element signals. (f) Silicon element signals.

(TEM) cross-section image and energy dispersive spectrometer (EDS) element analysis of the etched PBTTT film on a SiO<sub>2</sub>/Si substrate. The EDS scan starts from the carbon protection film (deposited on top of the PBTTT film) all the way to the substrate (see the arrow in Figure 2.4a). Although the TEM cross-section image and the carbon element signals in the EDS data hardly display the boundary between the carbon protection film and the etched PBTTT film, the sulfur element signals give us fingerprint information to clearly identify the PBTTT film in the EDS scan. The extracted thickness of the etched PBTTT film is 30 nm which is smaller than 40 nm of a pristine PBTTT film (measured previously by Kang et al.<sup>[39]</sup>).

Interestingly, the doping and etching processes did not affect the surface morphology of the PBTTT films. Figure 2.5 shows AFM images of the PBTTT films after



**Figure 2.5** (a) AFM image of the etched PBTtT film. (b) AFM image of the doped and unetched PBTtT film. (c) AFM image of the doped and etched PBTtT film.

both the doping and etching processes. Although the PBTtT film thickness was decreased from 40 nm to 30 nm by the etching, the surface images of both the etched PBTtT films in Figure 2.5a and c show the identical surface morphology as that of the pristine PBTtT film in Figure 2.2c. This result was one of the evidences that the PBTtT films were peeled off layer by layer during the argon plasma etching process. Furthermore, it was hard to identify additional features due to the dopant molecules on the PBTtT film surface after the doping.

## 2.2.2. Electrical characterization

The electrical characterization of the devices were performed using a semiconductor parameter analyzer (Keithley 4200 SCS) at a pressure of  $\sim 10^{-2}$  mbar in a vacuum probe station (JANIS Model ST-500).

## 2.2.3. Spectroscopy and microscopy

The UPS measurements were conducted by using AXIS SUPRA (Kratos, Inc.) at a base pressure of  $7 \times 10^{-9}$  mB with the He I photon line (21.22 eV) and the resolution

of 10 meV. The absorption spectra of the PBTTT films were acquired by using V-770 (JASCO). The TEM and EDS measurements were operated by JEM-2100F (JEOL) and the AFM images were scanned by NX-10 (Park systems).

#### 2.2.4. Contact resistance extraction by Y-function method

The Y-function method has been applied to field-effect transistors made of various materials including two-dimensional semiconductors for which the device geometry is typically hard to define, because this method only requires a single  $I_{DS}$ - $V_{GS}$  transfer curve in the linear regime ( $V_{GS} - V_{th} \gg V_{DS}$ ) for extracting the contact resistance.<sup>[52-54]</sup> In the linear regime,  $I_{DS}$  can be described as

$$\begin{aligned} I_{DS} &= \frac{W}{L} \mu_{eff} C_i (V_{GS} - V_{th}) V_{DS} \\ &= \frac{W}{L} \frac{\mu_0}{1 + \theta (V_{GS} - V_{th})} C_i (V_{GS} - V_{th}) V_{DS} \end{aligned}$$

where  $W$ ,  $L$ ,  $C_i$ ,  $\mu_{eff}$ ,  $\mu_0$  and  $\theta$  denote the channel length, the channel width, the capacitance per unit area, the effective mobility, the intrinsic mobility and the mobility attenuation factor. The mobility attenuation factor is described as

$$\theta = \theta_{ch} + \mu_0 C_i R_C \frac{W}{L} \approx \mu_0 C_i R_C \frac{W}{L} \quad (\text{for } V_{GS} - V_{th} \gg V_{DS})$$

where  $\theta_{ch}$  and  $R_C$  denote the attenuation factor from the channel and the contact resistance. In the large gate bias regime,  $\theta_{ch}$  is negligible compared to rest part of  $\theta$ .

The Y-function is defined by  $I_{DS}$  and the transconductance ( $g_m = \partial I_{DS} / \partial V_{GS}$ ) by

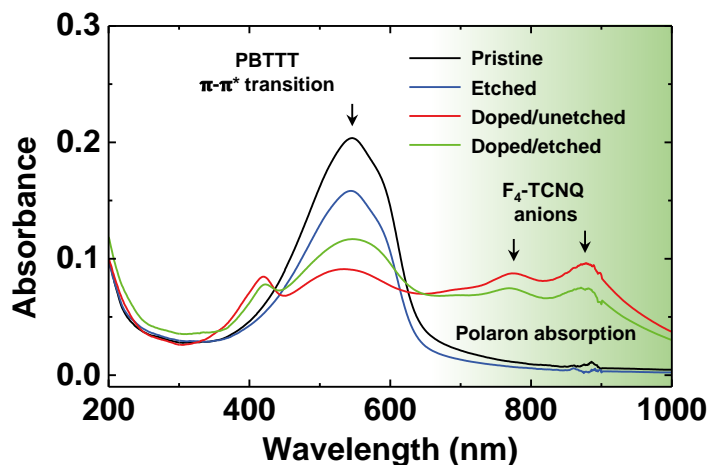
$$Y = \frac{I_{DS}}{\sqrt{g_m}} = \frac{I_{DS}}{\sqrt{\frac{W}{L} \frac{\mu_0}{(1 + \theta (V_{GS} - V_{th})^2} C_i V_{DS}}} = \sqrt{\frac{W}{L} \mu_0 C_i V_{DS} (V_{GS} - V_{th})}$$

Considering the slope of Y and  $1/\sqrt{g_m}$  with respect to  $V_{GS}$ , the slope of Y (denoted as  $S_y$ )

is  $\sqrt{\frac{W}{L}\mu_0C_iV_{DS}}$  and the slope of  $1/\sqrt{g_m}$  (denoted as  $S_g$ ) is  $\theta/\sqrt{\frac{W}{L}\mu_0C_iV_{DS}}$ . Therefore, the product of  $S_y^{-1}$ ,  $S_g$  and  $V_{DS}$  results in  $R_c$ .

## 2.3. Results and Discussions

### 2.3.1. Ultraviolet-visible absorption spectroscopy



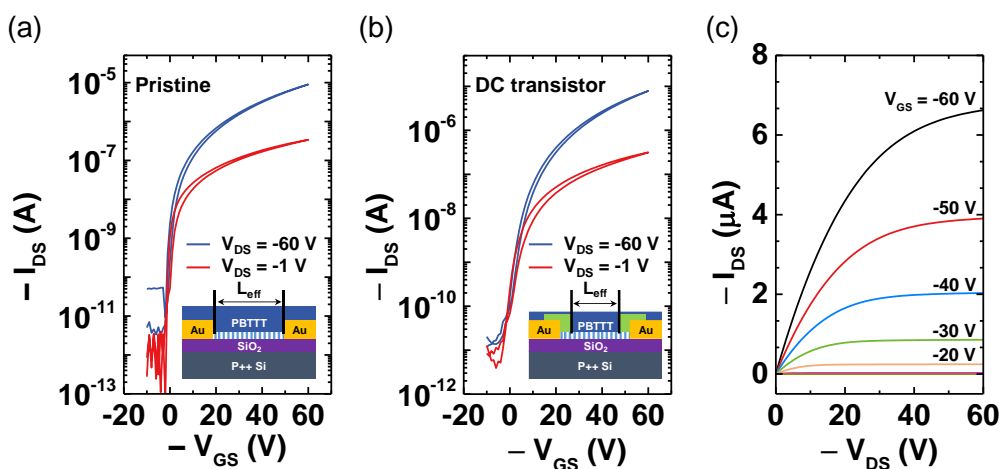
**Figure 2.6** UV-Vis spectra for pristine PBTtT, etched PBTtT, doped/unetched PBTtT, and doped/etched PBTtT films. The shaded area (in green) denotes a broad polaron absorption.

Figure 2.6 shows an ultraviolet-visible (UV-Vis) absorption data of various kinds of PBTtT films; a pristine (black line), etched (blue line), doped and unetched (denoted as “doped/unetched”, red line), and doped and etched (denoted as “doped/etched”, green line). Compared with the pristine film data, the etched film data show a decrease in the absorption over the entire range, while maintaining the surface morphology (Figure 2.5). This implies that the PBTtT films were peeled off layer by layer by the etching. By controlling the amount of F<sub>4</sub>-TCNQ dopant molecules with a nominal thickness of 10 nm, both the doped films data show that the amount of the neutral dopants on the film was much less than the previous research with a small peak near 400 nm which is a unique absorption feature of the neutral F<sub>4</sub>-TCNQ.<sup>[39]</sup> Furthermore, both the doped films data show a clear bleaching of the  $\pi$ - $\pi^*$  transition peak of PBTtT (resulting in a color change as seen from the right image

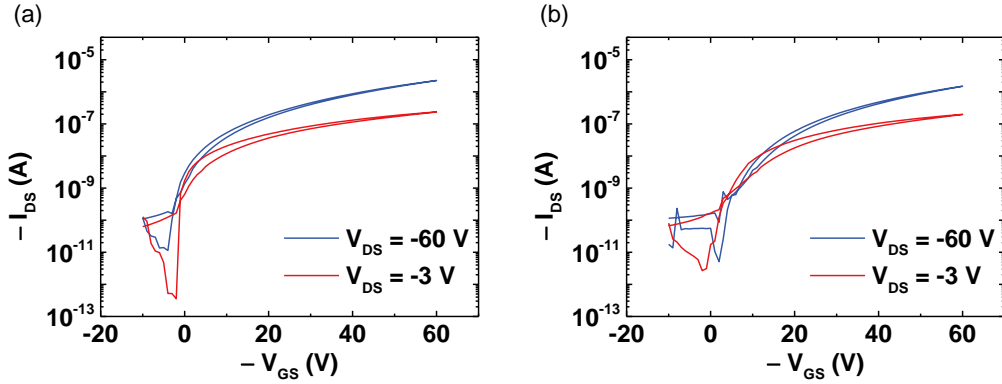
of Figure 2.3) and the appearance of distinct peaks corresponding to F<sub>4</sub>-TCNQ anion (near 780 and 890 nm). These results mean that the amount of the dopant molecules was considerably optimized, so most of the dopant molecules diffuse into the PBTTT without leaving too much neutral dopants. The shaded area (in green) of this UV-Vis plot indicates a broad polaron absorption in PBTTT.<sup>[55-56]</sup> The doped/etched film data show a slight recovery of the  $\pi$ - $\pi^*$  transition peak of PBTTT, and a shrinkage of the neutral F<sub>4</sub>-TCNQ and F<sub>4</sub>-TCNQ anion peaks near 400 nm and 800 nm, respectively. These results imply that the etching caused a slight de-doping at the top surface of the doped PBTTT films by preferential etching of the dopant molecules (as shown in the final step of the fabrication process in Figure 2.1a).

### 2.3.2. Electrical characterization of PBTTT OFETs

Figure 2.7a and b shows the transfer curve of the 50  $\mu\text{m}$  channel length transistors for both the linear and saturation regimes. The doped contact (i.e., doped/etched, donated as “DC”) PBTTT transistors showed the ON/OFF ratio over than  $10^5$  with the mobility of

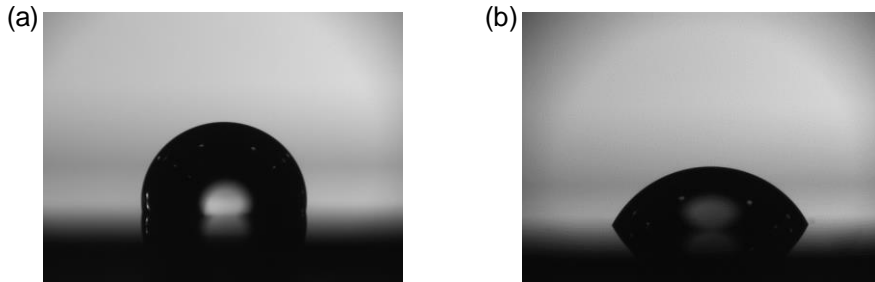


**Figure 2.7**  $I_{DS}$ - $V_{GS}$  transfer curves of (a) the pristine and (b) doped contact (doped/etched) PBTTT transistor. (c)  $I_{DS}$ - $V_{DS}$  output curves of a doped contact (doped/etched) PBTTT transistor.



**Figure 2.8**  $I_{DS}$ - $V_{GS}$  transfer curves of the pristine PBTTT transistor (a) before etching and (b) after etching.

0.045  $\text{cm}^2/\text{V}\cdot\text{s}$ . I extracted the field-effect mobility from the transfer curve from the following equation,  $I_{DS} = \frac{\mu W C_i}{2L_{eff}} (V_{GS} - V_{th})^2$  in saturation regime, where  $W$ ,  $L_{eff}$ ,  $C_i$ ,  $\mu$  and  $V_{th}$  denote the channel width, the channel length, the capacitance per unit area, the mobility and the threshold voltage of PBTTT transistors. Compared with the pristine devices with the mobility of 0.053  $\text{cm}^2/\text{V}\cdot\text{s}$ , DC PBTTT transistors had a slightly lower mobility, which was caused by the etching process. This is supported by a slight decrease in the mobility of the pristine PBTTT OFETs from 0.060  $\text{cm}^2/\text{V}\cdot\text{s}$  to 0.051  $\text{cm}^2/\text{V}\cdot\text{s}$  after the etching process (Figure 2.8). Although the surface morphology was not changed by the etching, the water contact angle of the PBTTT films was changed from  $101.7^\circ$  to  $67.3^\circ$ ,

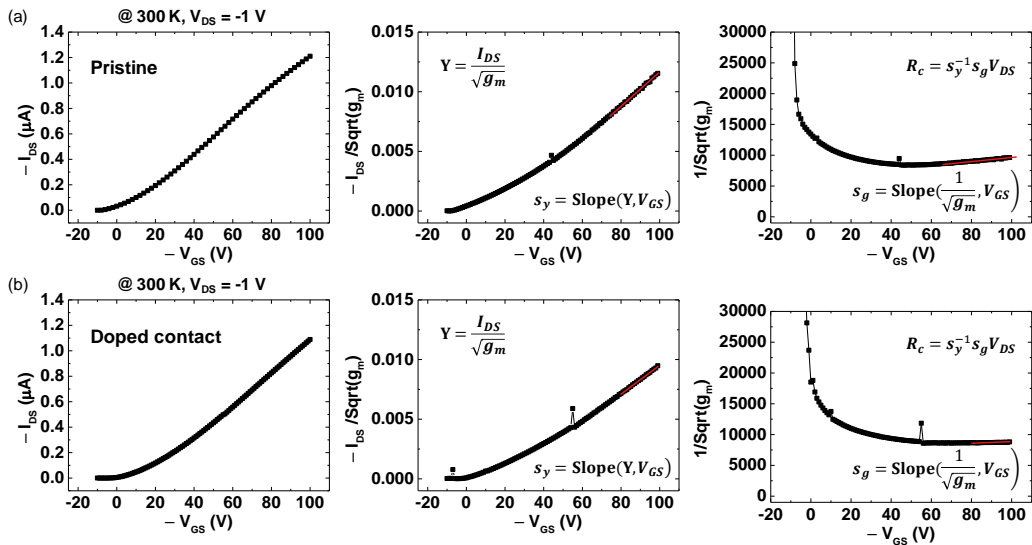


**Figure 2.9** (a) A water droplet on a pristine PBTTT film. (b) A water droplet on an etched PBTTT film.



which can imply a slight change of chemical properties of the film surface (Figure 2.9).

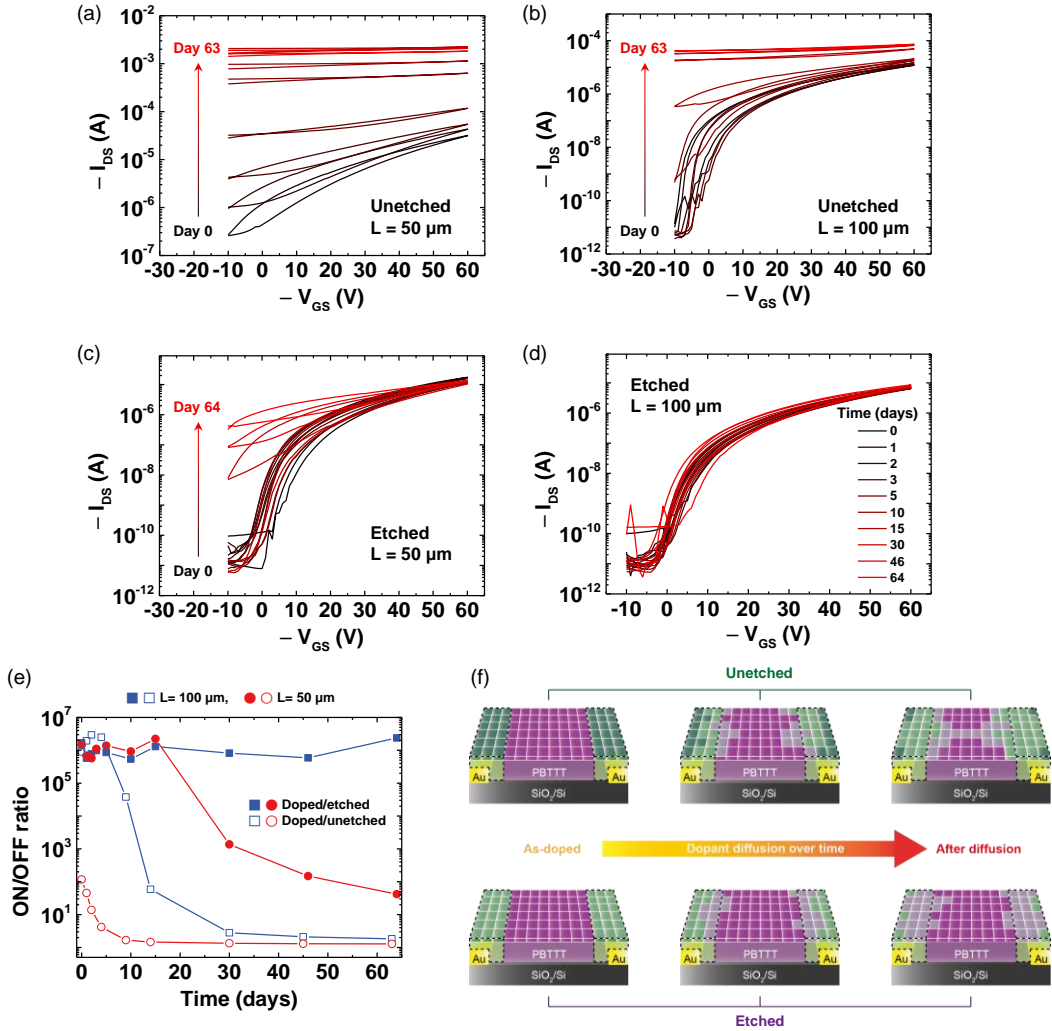
Figure 2.7c shows the  $I_{DS}$ - $V_{DS}$  output curves of DC transistors which represents favorable output characteristics without the S-shape at a low  $V_{DS}$  regime that is typically induced by a significant contact resistance. From the Y-function method, the extracted value of the contact resistance of DC PBTTT transistors from the data in Figure 2.10 was found to be  $5.1 \text{ k}\Omega \cdot \text{cm}$  and that of pristine device was found to be  $24.5 \text{ k}\Omega \cdot \text{cm}$ . The contact resistance of DC PBTTT transistor had a comparable value to the lowest value that has been reported in literature.<sup>[32,57]</sup>



**Figure 2.10**  $I_{DS}$ - $V_{GS}$  transfer curves, Y-function and  $1/\sqrt{g_m}$  plotted with  $V_{GS}$  for (a) the pristine PBTTT transistor and (b) the doped contact PBTTT transistor.

### 2.3.3. ON/OFF ratio stability of the doped-contact PBTTT OFETs

The etching process was an essential step for reducing the amount of the neutral dopants and improving the stability of the devices. Figure 2.11e shows the ON/OFF ratio of the doped PBTTT transistors either etched (filled symbols) or unetched (empty symbols),

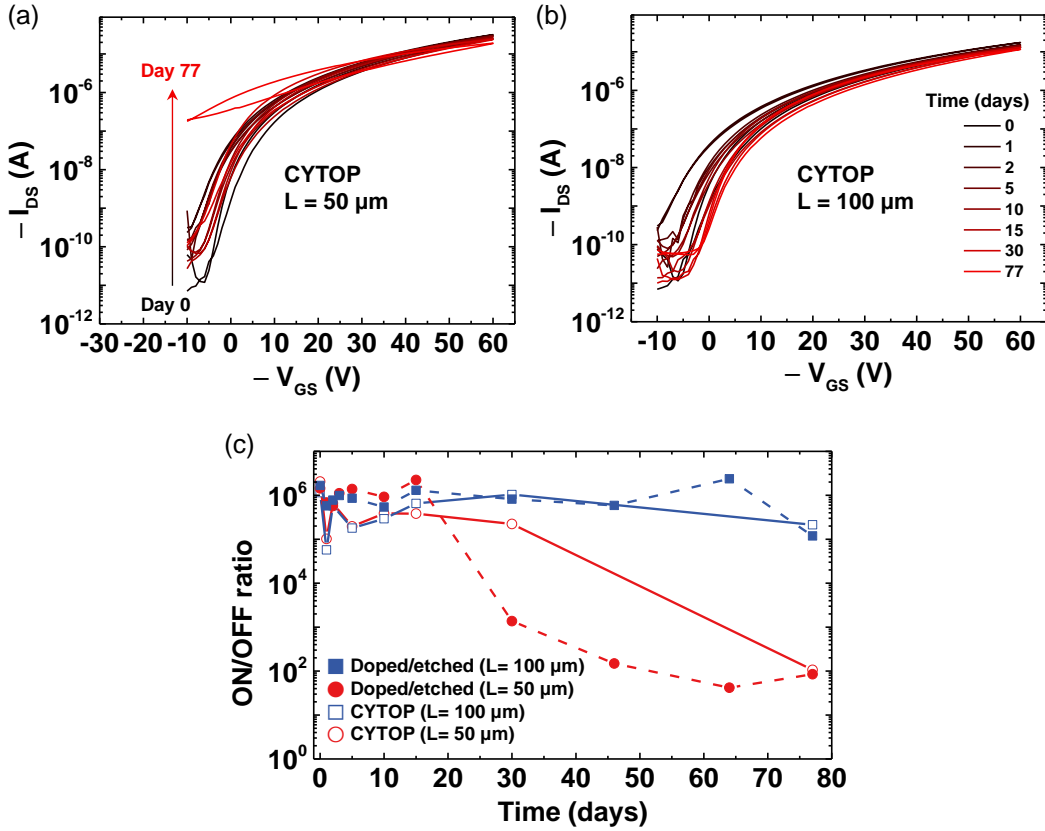


**Figure 2.11** The time evolution of transfer curves for (a) the doped/unetched PBTTT transistor with the channel length,  $L_{\text{ch}}$ , of  $50 \mu\text{m}$ , (b) the doped/unetched PBTTT transistor with  $L_{\text{ch}} = 100 \mu\text{m}$ , (c) the doped contact (doped/etched) PBTTT transistor with  $L_{\text{ch}} = 50 \mu\text{m}$ , and (d) the doped contact PBTTT transistor with  $L_{\text{ch}} = 100 \mu\text{m}$  for two months. (e) ON/OFF ratio stability for the doped PBTTT transistors with a channel length ( $L$ ) of  $50 \mu\text{m}$  and  $100 \mu\text{m}$ . (f) Schematic images of doped region propagation by the neutral dopants diffusion.

measured over the time scale of two months. For the doped transistors with the channel length of  $50 \mu\text{m}$ , the doped/etched devices preserved its ON/OFF ratio over  $10^5$  for about

15 days, whereas it was difficult to define the ON/OFF ratio for the doped/unetched devices just after fabrication due to a large off-current. For the channel length of 100  $\mu\text{m}$ , the doped/etched devices preserved its ON/OFF ratio for more than two months, on the other hand the ON/OFF ratio of the doped/unetched devices dropped significantly after 15 days. The decrease of the ON/OFF ratio was mainly caused by orders of magnitude increase in the off-current. Figure 2.11f shows a schematic diagram that depicts different propagation rates of the doped region in the doped/unetched and doped/etched devices over time based on optical images of the doped region propagation (see Figure 2.13 in Chapter 2.3.4.). The different propagation rates mainly result from different diffusion rates of the neutral dopant molecules, which have been shown to be much more diffusive than ionized dopant molecules.<sup>[58-59]</sup> The figure represents the possible formation of percolated current paths between the source and drain electrodes (i.e. the doped regions from each side meet in the middle) which would result in the rise of the off-current. The diffusion of the neutral dopant molecules takes place in both the doped/unetched and doped/etched devices, but such diffusion effect is less significant for the doped/etched device due to a lower initial amount of the neutral dopants. Therefore, percolation paths are much more difficult to form in the doped/etched device. In the next section, this concept could be verified by a numerical simulation which has been applied to reveal the diffusion velocity of molecules in various systems.<sup>[60-61]</sup> A modified Fick's diffusion equation was solved by a numerical simulation that accounts for the capturing of diffusive neutral dopant molecules via charge transfer.

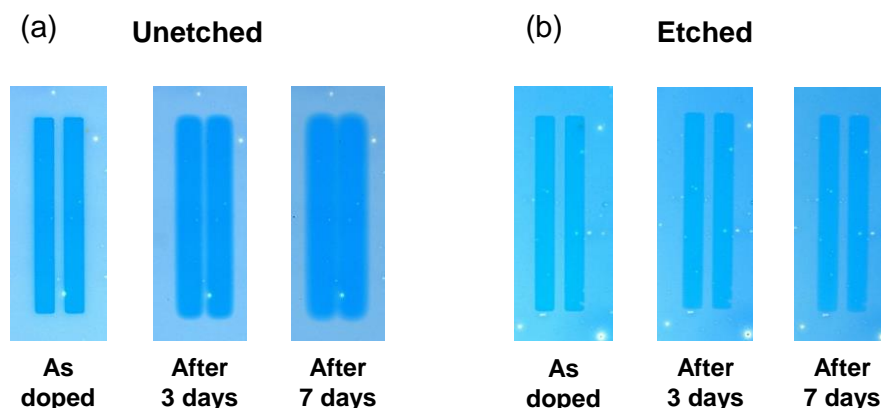
I also discovered that the surface diffusion of the neutral dopants would be prohibited further by introducing a dielectric layer on top of the doped/etched PBTTT film. Figure 2.12 shows the ON/OFF ratio of the DC PBTTT transistors encapsulated with a



**Figure 2.12**  $I_{DS}$ - $V_{GS}$  transfer curves of (a) the CYTOP encapsulated doped contact PBTtT transistor with the channel length of 50  $\mu\text{m}$  and (b) the CYTOP encapsulated doped contact PBTtT transistor with the channel length of 100  $\mu\text{m}$  for more than two months. (c) The ON/OFF ratio stability for the doped contact and CYTOP encapsulated doped contact transistors.

CYTOP (CTL-809M, Asahi Glass) layer on top showed a greater stability over time for the devices with 50  $\mu\text{m}$  channel length, compared to the DC devices without any layers on top (see Figure 2.12c). This result would be an evidence that the neutral dopant molecules diffuse primarily along the surface. A detailed investigation of a microscopic mechanism for the surface interaction between the CYTOP molecules and neutral dopants is beyond the scope of this study.

### 2.3.4. Numerical simulation of the diffusion of F<sub>4</sub>-TCNQ



**Figure 2.13** Optical images of the rectangular doped regions with the 50  $\mu\text{m}$  gap in the (a) doped/unetched and (b) doped/etched PBT film for one week.

As discussed in the previous section, the dopant diffusion is a critical issue that has to be solved for the ON/OFF ratio stability of the doped transistors. The dopant diffusion can be visually observed from the optical images of the selectively doped PBT films with the same shadow mask used for doped transistors with the channel length of 50  $\mu\text{m}$  (see Figure 2.13a). The doped regions (darker regions) propagate over time, blurring the rectangular edges. After seven days, the 50  $\mu\text{m}$  gap was nearly filled with the propagated doped regions in the doped/unetched case. In order to mitigate the diffusion problem, I introduced argon plasma etching to control the amount of the dopant molecules in the PBT film, which suppressed the propagation of the doped region significantly (see Figure 2.13b). In the doped/etched case, the 50  $\mu\text{m}$  gap could be clearly distinguished over one week. Therefore, I considered that the propagation of the doped regions from the source and drain electrodes was the reason of the rise of the off-current for the doped PBT transistors. To understand the propagation of the doped region, I constructed a solid-state diffusion model of F<sub>4</sub>-TCNQ molecules in PBT film and performed numerical

simulations to confirm the validity of our model.

Before discussing the diffusion of F<sub>4</sub>-TCNQ molecules in PBTTT film, I will briefly discuss the processes involved in the molecular doping of PBTTT by F<sub>4</sub>-TCNQ molecules. Charge-transfer doping between a host donor molecule and a strong acceptor molecule (i.e. a high electron affinity like F<sub>4</sub>-TCNQ) is known to undergo integer-charge transfer (ICT), leading to a complete transfer of an electron from the host to the acceptor.<sup>[62-63]</sup> The molecular doping in organic semiconductors via ICT was recently proposed to occur in two steps; in the first step, a single-electron transfer from donor to acceptor molecules making a integer-charge transfer complex (ICTC) and in the second step, the dissociation of the ICTC resulting in mobile polarons.<sup>[64]</sup> Then, the formation of ICTC via charge transfer reaction could be described as the following reaction formula



where  $[D]$ ,  $[A]$  and  $[D^+A^-]$  denote the concentration of the donor molecules, the concentration of the acceptor molecules and the concentration of ICTC. In this study, a PBTTT host molecule was a donor and a F<sub>4</sub>-TCNQ dopant molecule was an acceptor. Therefore, a complete doping process will produce a F<sub>4</sub>-TCNQ anion and a mobile hole in PBTTT. However, since the dopant concentration was quite comparable with the host concentration, not all the F<sub>4</sub>-TCNQ molecules undergo charge transfer but there remain some unreacted dopant molecules (i.e. neutral dopant molecules) in the PBTTT film. After the ionization of the dopant molecules during ICT, there is an electrostatic force between the F<sub>4</sub>-TCNQ anions and holes in the PBTTT film. Therefore, I considered that the likelihood of F<sub>4</sub>-TCNQ anion diffusion was much lower than that of the neutral F<sub>4</sub>-TCNQ molecule diffusion in PBTTT. In addition, the amount of the neutral dopant molecules will be especially large near the top surface of PBTTT as previously observed from the depth-

profile of the molecular ratio between F<sub>4</sub>-TCNQ and PBTTT.<sup>[39]</sup> Therefore, I assumed that the dominant contribution towards the diffusion is from the neutral dopant molecules near the top surface of the PBTTT film. Recently, this was verified by spectroscopic measurement of the sequentially p-doped P3TH by Reiser et al.<sup>[58]</sup>

In order to simulate the solid-state diffusion of neutral F<sub>4</sub>-TCNQ molecules in PBTTT, I modified Fick's second law in a one-dimensional (1D) case considering a finite capturing of the neutral F<sub>4</sub>-TCNQ molecules by charge transfer reaction as described above. A modified 1D Fick's second law would be expressed as

$$\frac{\partial[N]}{\partial t} = D \frac{\partial^2[N]}{\partial x^2} - f \quad (2)$$

where  $[N]$ ,  $D$  and  $f$  denote the neutral dopant concentration, the diffusion constant and a function representing the rate of the capturing process, respectively. The form of  $f$  will be described in details later. Designating the increment of time and space as  $\Delta t$  and  $\Delta x$ , then, in simulation, Equation (2) is converted to

$$\frac{[N]_x^{t+\Delta t} - [N]_x^t}{\Delta t} = D \frac{[N]_{x+\Delta x}^t + [N]_{x-\Delta x}^t - 2[N]_x^t}{\Delta x^2} - f \quad (3)$$

where  $[N]_x^t$  denotes the value of  $[N]$  at the time coordinate,  $t$ , and space coordinate,  $x$ . To construct  $f$ , I assumed that the dominant capturing process is the reaction via charge transfer as described in Equation (1). Then, the generation rate of the ICTC concentration ( $[P^+N^-]$ ) can be expressed as  $d[P^+N^-]/dt$  in terms of a second-order rate equation that depends on both the concentration of the unreacted PBTTT concentration ( $[P]$ ) and  $[N]$ :

$$\frac{d[P^+N^-]}{dt} = k[P][N] \quad (4)$$

where  $k$  is the rate constant of the reaction. Following the Equation (1), the increasing amount of  $[P^+N^-]$  is equal to the decreasing amount of  $[N]$ . Therefore, I could describe  $f$  as the following:

$$f([N]_x^t, [P]_x^t) = k[P]_x^t[N]_x^t \quad (5)$$

Then, the change of ICTC concentration is converted to

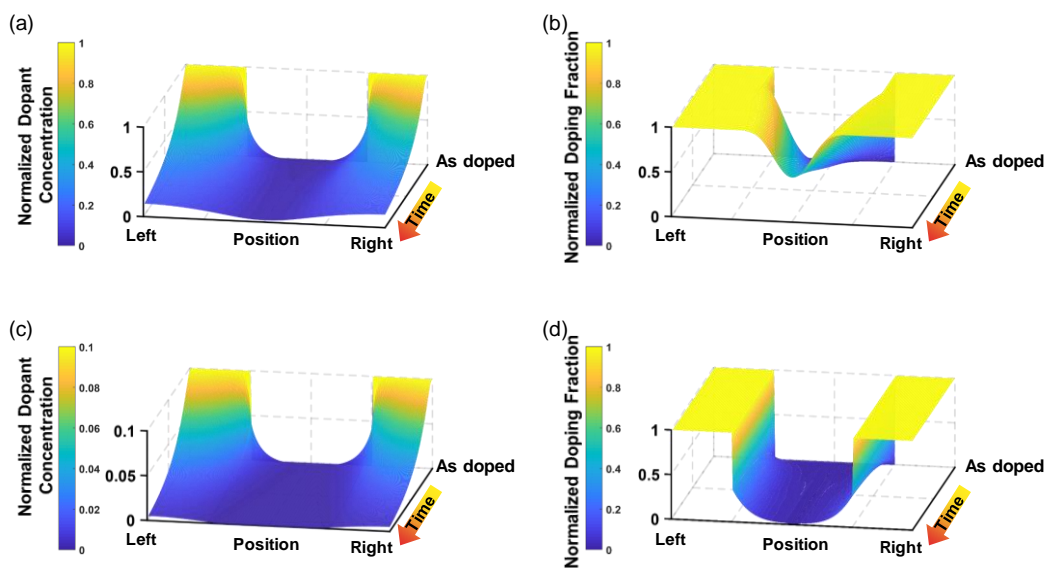
$$[P^+N^-]_x^{t+\Delta t} - [P^+N^-]_x^t = \Delta t k [P]_x^t [N]_x^t \quad (6)$$

$[P^+N^-]$  is equal to F<sub>4</sub>-TCNQ anion concentration assuming that the charge transfer process is ICT, which is most likely to be true for this case since the ionization potential of PBTTT is smaller than the electron affinity of F<sub>4</sub>-TCNQ.<sup>[64]</sup> Estimating the exact values of  $k$  and  $D$  requires advanced experimental techniques that could spatially map  $[N]$  and  $[P^+N^-]$  in the channel of the device, which is beyond the scope of this study. However, I were able to qualitatively predict the time evolution of the doped region propagation in the channel of the doped PBTTT transistors by predicting  $[N]$  and  $[P^+N^-]$  from this numerical calculation.

Since  $[P^+N^-]$  could represent the doped PBTTT concentration, I normalized  $[P^+N^-]_x^t$  by the concentration of total PBTTT molecules to calculate the doping fraction of PBTTT molecules at the space coordinate,  $x$ , at time,  $t$ . Following the assumption that the rise in the OFF current is caused by the formation of percolated current paths between the source and drain electrodes, there exists a critical doping fraction in the middle of the channel for forming the conduction paths between the electrodes. Therefore, if the doping fraction in the middle of devices exceeds a particular value, I consider that the increase of the off-current causes the ON/OFF ratio of the devices to decrease. In the simulation, the initial value of the neutral dopant is set (i.e.  $[N]$  at  $t = 0$ ) over a certain width at both sides of the channel of doped transistors in order to describe the doped regions beside source and drain electrodes in the devices just after the fabrication. During the simulation, the neutral dopant molecules from both sides of the channel diffuse towards the middle, some of which are captured during the diffusion. In order to investigate the effect of the

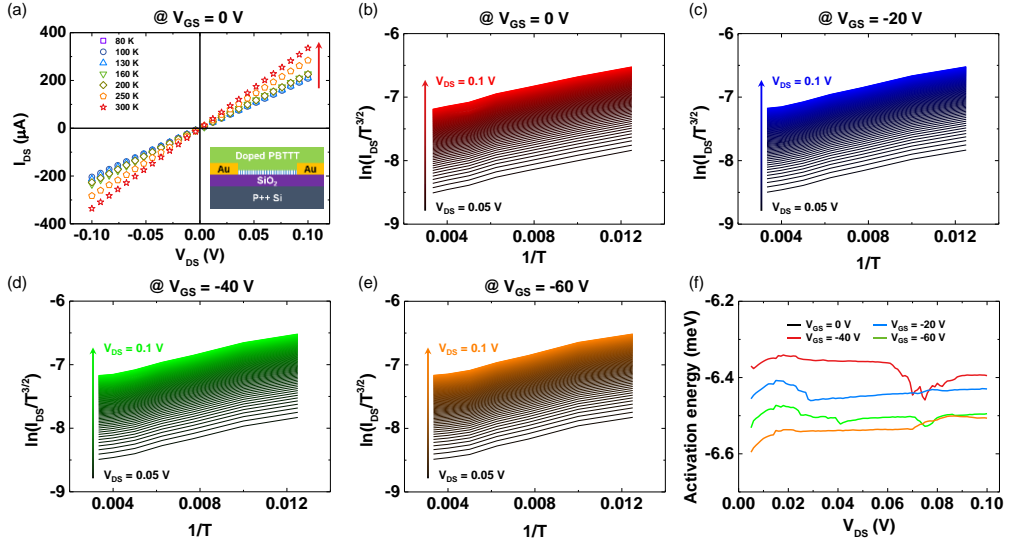


argon plasma etching on the propagation of the doped regions, the only controlled parameter that I varied between the doped/unetched and doped/etched cases was the initial amount of the neutral dopants; the initial amount neutral dopant of the doped/unetched device is ten times of that of the doped/etched device. Figure 2.14 shows the spatial distribution of the neutral dopant concentration and the doping fraction of the PBTTT molecules over time. Although the only input parameter that varied between the doped/unetched and doped/etched cases was the initial amount of the neutral dopants, the doping fraction profiles show clear contrasts between the two cases in Figure 2.14b and d. Especially, I found that the doping fraction at the center of the PBTTT film (i.e. an indicator for the formation of the percolated current paths) was negligible for the doped/etched case whereas the doping fraction gradually increased over time for the doped/unetched case.



**Figure 2.14** (a) The evolution of the neutral dopant concentration of the doped/unetched device. (b) The evolution of the doping fraction of the PBTTT molecules of the doped/unetched device. (c) The evolution of the neutral dopant concentration of the doped/etched device. (d) The evolution of the doping fraction of the PBTTT molecules of the doped/etched device.

### 2.3.5. Band diagram analysis

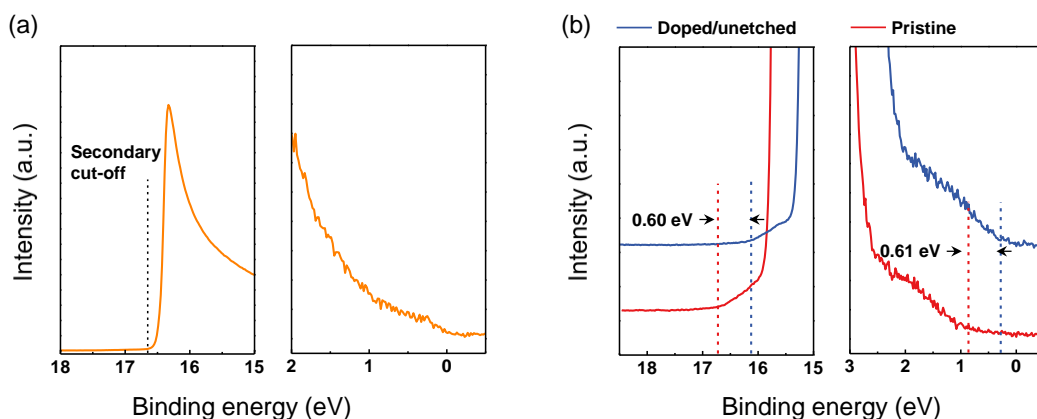


**Figure 2.15** (a)  $I_{DS}$ - $V_{DS}$  output curves of an entire-doped PBTTT device at  $V_{GS} = 0$  V in a temperature range from 80 K to 300 K. (b)  $\ln(I_{DS}/T^{3/2})$  vs  $1/T$  at  $V_{GS} = 0$  V. (c)  $\ln(I_{DS}/T^{3/2})$  vs  $1/T$  at  $V_{GS} = -20$  V. (d)  $\ln(I_{DS}/T^{3/2})$  vs  $1/T$  at  $V_{GS} = -40$  V. (e)  $\ln(I_{DS}/T^{3/2})$  vs  $1/T$  at  $V_{GS} = -60$  V. (f) The plots of activation energies vs  $V_{DS}$ .

To confirm the doping effect on the carrier injection properties directly, I fabricated homogeneously doped (i.e., entire PBTTT area in a transistor is doped and etched; denoted as “entire-doped”) PBTTT devices with the channel length of  $2 \mu\text{m}$  by a conventional photolithography. Figure 2.15a shows the  $I_{DS}$ - $V_{DS}$  data of an entire-doped device measured from 80 K to 300 K. For this temperature range, the entire-doped device showed a clear ohmic behavior. This result implies that the charge injection occurred without an activation barrier. Since two-dimensional (2D) charge transport properties in PBTTT have been previously demonstrated,<sup>[39,65]</sup> the thermionic emission equation for 2D semiconducting

system,  $I_{DS} = R^* T^2 \exp[-(q/k_B T)(\phi - V_{DS}/\eta)]$ , was employed to extract the activation energy of the contact between the doped PBTTT and gold electrodes, where  $R^*$ ,  $\phi$ , and

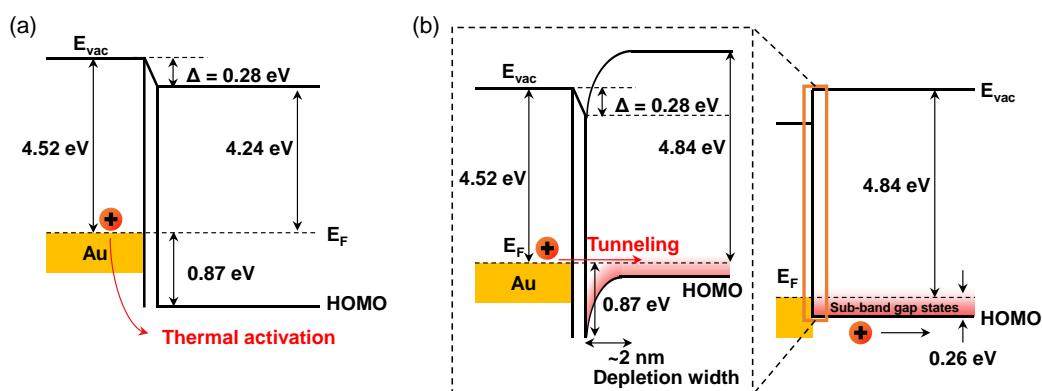
$\eta$  denote the Richardson coefficient, the effective activation energy, and ideality factor, respectively. The curves of  $\ln(I_{DS}/T^{3/2})$  vs  $1/T$  were plotted for each  $V_{DS}$  bias under the gate bias from 0 V to  $-60$  V as shown in Figure 2.15b to e. The extracted activation energies, by using the slopes of  $\ln(I_{DS}/T^{3/2})$  vs  $1/T$  plots for each  $V_{DS}$  bias, are plotted as shown in Figure 2.15f. The effective activation energy was determined as the extrapolated value of the activation energy at  $V_{DS} = 0$  V. For all gate biases, the extracted thermal activation energy had negative values, which implies that a dominant charge injection mechanism was not likely to be thermionic emission.



**Figure 2.16** (a) The UPS data of 50 nm-thick Au films near the Fermi level and secondary-electron cut-off. (b) The UPS data of the doped/unetched and pristine PBTBT films near the Fermi level (right) and secondary-electron cut-off (left).

To construct the band diagram of the contact region of the devices, ultraviolet photoelectron spectroscopy (UPS) was conducted for both the pristine and doped/unetched PBTBT films. The Fermi levels of these samples were calibrated by the UPS data of 50 nm thick gold film and the value of the work function of gold was determined to be 4.52 eV (Figure 2.16a). This value is slightly less than the typical 5.0 eV reported for gold presumably due to a low vacuum level ( $\sim 10^{-7}$  torr) used during the evaporation.<sup>[66-67]</sup> Here,

I used the doped/unetched PBTTT film for UPS data since I assume that the PBTTT molecules at the bottom side of devices were free from etching. Figure 2.16b shows the UPS spectra for binding energies near the Fermi level and secondary-electron cut-off region. The UPS data showed similar shifts for both the highest occupied molecular orbital (HOMO) levels and secondary-electron cut-off levels of the PBTTT films after doping. The difference between the Fermi level and the HOMO level of the PBTTT film was reduced from 0.87 eV to 0.26 eV after doping.

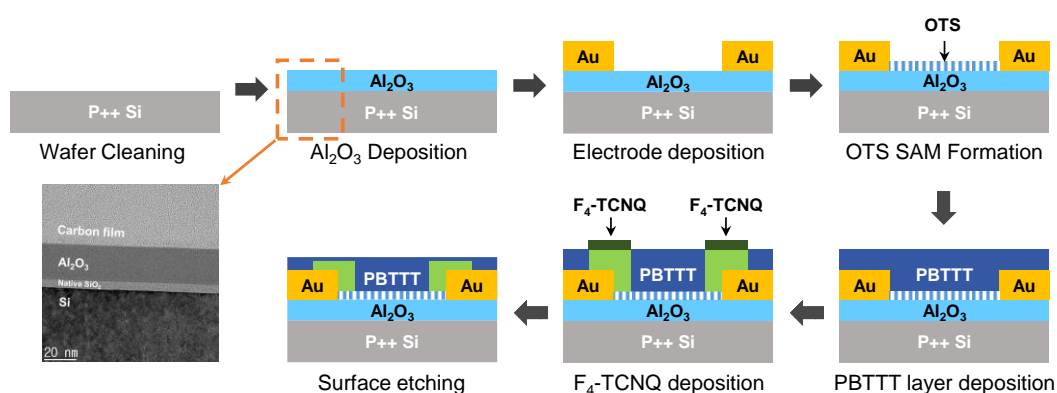


**Figure 2.17** The band diagram near the contact of (a) the pristine PBTTT transistor and (b) the doped contact PBTTT transistor, with a highlighted view of the band diagram at the contact.

Figure 2.17a and b show the band diagrams near the contact electrodes for the pristine and doped PBTTT molecules, based on the UPS analysis. I regarded that the interface dipole caused a vacuum level shift of 0.28 eV between the gold electrode and the PBTTT films.<sup>[68]</sup> Considering the charge concentration of the doped PBTTT film of about  $3.3 \times 10^{20} \text{ cm}^{-3}$ ,<sup>[39]</sup> the depletion width between the doped PBTTT and gold is about 2 nm which is thin enough for tunneling.<sup>[35]</sup> From the  $I_{DS}-V_{DS}$  data of an entire-doped device and band diagram analysis, I considered that the charge injection of the devices was enhanced since the dominant charge injection mechanism was changed from thermionic

emission (pristine transistors) to thermally assisted tunneling (doped contact transistors) via the doping of contact regions. Despite of the 0.26 eV energy gap between the gold electrodes and the doped PBT TT molecules (Figure 2.17b), this contact showed ohmic properties as shown in Figure 2.15a. This may be due to sub-band gap states induced by doping which are accessible by injected charges from the electrodes via tunneling.

### 2.3.6. Low-voltage operation OFETs by using high-k dielectric

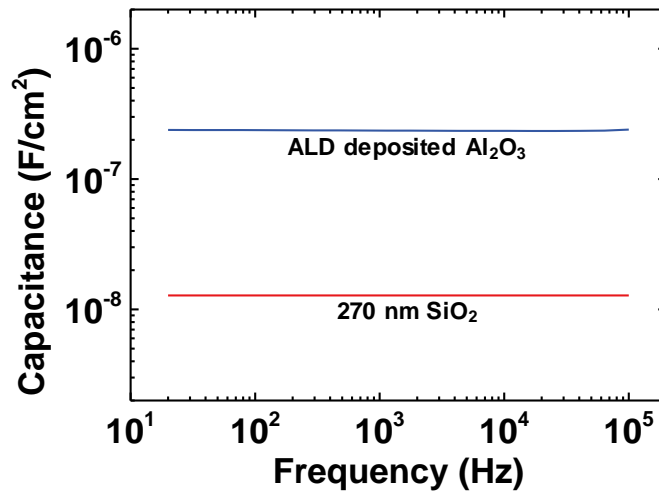


**Figure 2.18** The fabrication process of the high-k PBT TT transistors on Al<sub>2</sub>O<sub>3</sub>.

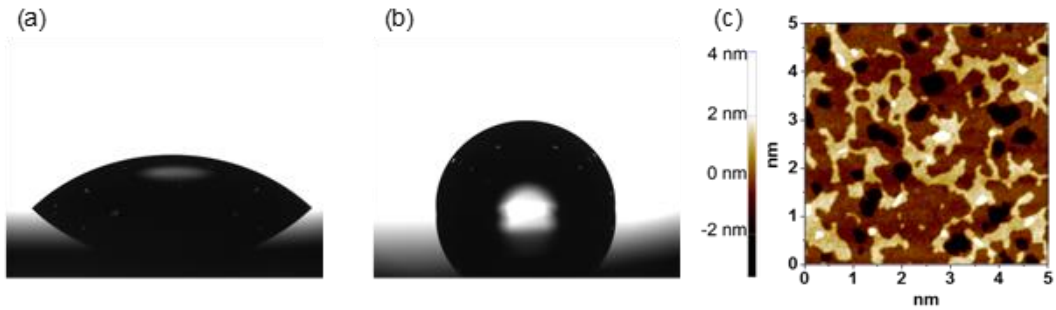
A crucial advantage of the bottom-gate structure employed in the study comes from its extra degree of freedom in the choice of the dielectric material that is compatible with the semiconductor. This is highly relevant for OFETs with high-k dielectric materials which typically require relatively high temperature processes which results in irreversible damages to the OSC film, as well as exposure to chemical environments which can harm the OFET device performance (e.g. exposure to water during atomic layer deposition (ALD)).<sup>[69]</sup> Therefore, in order to use high-k dielectric materials for low-voltage operation of OFETs, the dielectric materials should be ideally deposited before the OSCs. To demonstrate the advantage of the molecular implantation doping in the low-voltage

operation of OFETs, I adopted  $\text{Al}_2\text{O}_3$  as the bottom gate dielectric deposited by ALD. Figure 2.18 illustrates the fabrication process of the high-k devices. After Si substrates were cleaned using de-ionized water, isopropanol and acetone for 10 min in each cleaning solvent by sonication in an ultrasonic bath, the substrates were further cleaned with an oxygen plasma etching (50 W for 2 min). After the substrate cleaning,  $\text{Al}_2\text{O}_3$  layers were deposited on the substrates by an atomic layer deposition (ALD) for 200 cycles at a pressure of  $\sim 10^{-1}$  torr. The thickness of the deposited  $\text{Al}_2\text{O}_3$  was 25 nm on 5 nm  $\text{SiO}_2$  native oxide of a Si substrate (TEM image in Figure 2.18). The rest of the fabrication processes was identical to the process described in Section 2.2.1.

Figure 2.19 shows the measured capacitance data of the deposited  $\text{Al}_2\text{O}_3$ . The capacitance value was measured by LRC meter (4248A, Hewlett Packard) and the value was  $2.36 \times 10^{-7} \text{ F/cm}^2$ . The measured values are reasonable considering the thicknesses and the dielectric constants of the deposited  $\text{Al}_2\text{O}_3$  and native  $\text{SiO}_2$  (25 nm thick  $\text{Al}_2\text{O}_3$  and a 5 nm thick native  $\text{SiO}_2$  on a silicon substrate from Figure 2.18). This measured



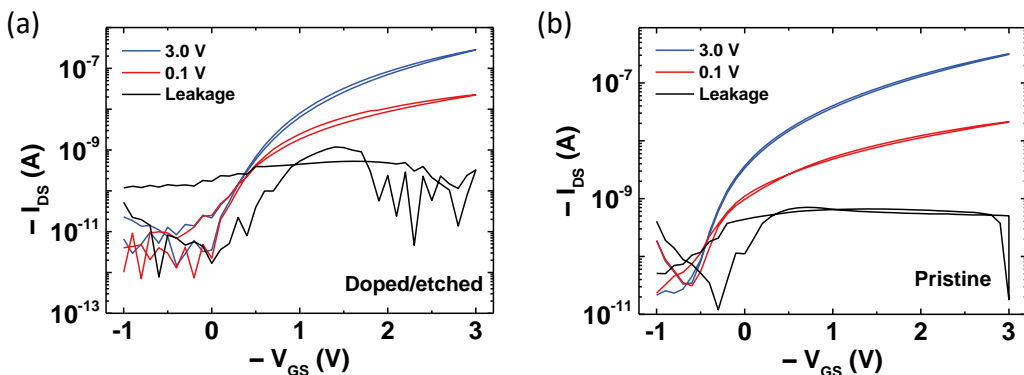
**Figure 2.19** The measured capacitance data of the deposited  $\text{Al}_2\text{O}_3$ . The calculated capacitance value of 270 nm  $\text{SiO}_2$  is displayed in below for comparison.



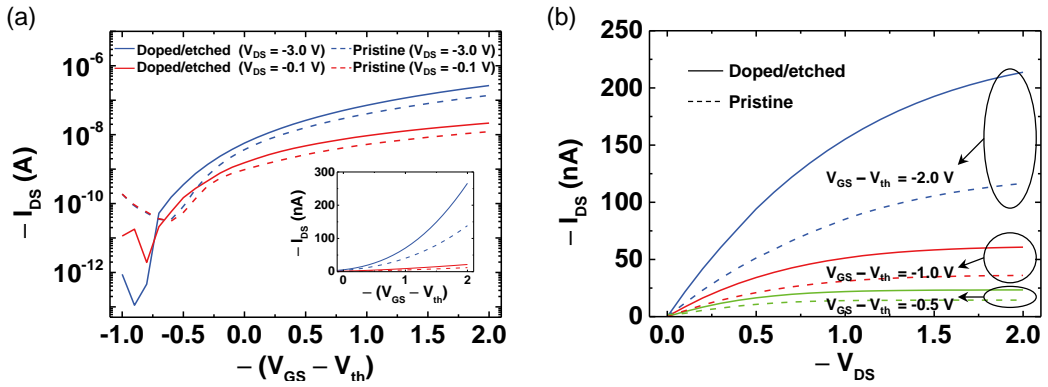
**Figure 2.20** (a) A water droplet on a pristine  $\text{Al}_2\text{O}_3$  substrate. (b) A water droplet on the OTS SAM treated  $\text{Al}_2\text{O}_3$  substrate. (c) AFM image of the PBTtT film deposited on the OTS SAM treated  $\text{Al}_2\text{O}_3$  substrate.

capacitance value is about 18 times higher than the capacitance value for the 270 nm thick  $\text{SiO}_2$  ( $1.28 \times 10^{-8} \text{ F/cm}^2$ ) used in Figure 2.1a.

Figure 2.20 shows the OTS SAM treatment showed an excellent improvement of the interface like in the  $\text{SiO}_2$  case in terms of the PBTtT film morphology which is critical to the PBTtT OFET performance.<sup>[70]</sup> As a result, the DC PBTtT transistors on  $\text{Al}_2\text{O}_3$  had a similar mobility value to those on  $\text{SiO}_2$ . The transfer curves did not show a significant hysteresis which is usually induced by trap sites on the gate dielectric interface (Figure 2.21).



**Figure 2.21** (a) The  $I_{DS}-V_{GS}$  transfer curve of the doped contact transistor and (b) the pristine transistor with OTS SAM treated  $\text{Al}_2\text{O}_3$ . The black lines represent the gate leakage current in the devices.



**Figure 2.22** (a)  $I_{DS}$ - $V_{GS}$  transfer curves of the doped contact and pristine PBTtT transistors. Linear plots of the output curves are shown in the inset. (b)  $I_{DS}$ - $V_{DS}$  output curves of the doped contact and pristine PBTtT transistors.

Figure 2.22 shows  $I_{DS}$ - $V_{GS}$  transfer characteristics of the pristine and the DC PBTtT transistors on  $\text{Al}_2\text{O}_3$  gate dielectrics with the channel length of 50  $\mu\text{m}$ . All of the voltage biases were under 3 V to avoid dielectric breakdown.<sup>[71]</sup> The DC PBTtT device had about twice the value of  $I_{DS}$  value than the pristine one in both the linear and saturation regimes. Interestingly, these results indicate that the DC PBTtT devices had a larger mobility than the pristine devices; 0.037  $\text{cm}^2/\text{V}\cdot\text{s}$  for DC PBTtT devices and 0.019  $\text{cm}^2/\text{V}\cdot\text{s}$  for pristine devices. These results show that the reduction of the contact resistance is more effective in the low-voltage operation of the OFETs which could be applied to low power consumption organic electronics.



## 2.4. Conclusion

In conclusion, I demonstrated an enhanced charge injection in PBTTT OFETs by molecular implantation doping with F<sub>4</sub>-TCNQ and introduced an argon plasma etching treatment for improving the off-current stability. With this approach, the amount of neutral dopants was effectively controlled and the dopant diffusion into the active channel of the PBTTT OFETs was significantly suppressed. If the neutral dopants are removed completely by further optimization, this technique could work even for devices with smaller channel length. The low temperature measurement and the band diagram analysis implied that the enhanced charge injection properties originated from the change of the dominant charge injection mechanism from thermionic emission to tunneling at the contact between the doped PBTTT films and metal electrodes. In addition, I demonstrated the low-voltage operation devices by using Al<sub>2</sub>O<sub>3</sub> as a high-k gate dielectric material. For the high-k devices, the doped contact PBTTT transistor showed a better performance compared to the pristine devices. This study provides clear evidences that the molecular implantation doping is potentially one of the key techniques for solving the contact resistance issue for OFETs, thereby facilitating low-power organic electronics.

## References

- [1] X. Gu, L. Shaw, K. Gu, M. F. Toney, Z. Bao, *Nat. Commun.* **2018**, 9, 534.
- [2] W.-Y. Lee, H.-C. Wu, C. Lu, B. D. Naab, W.-C. Chen, Z. Bao, *Adv. Mater.* **2017**, 29, 1605166.
- [3] T. Someya, Z. Bao, G. G. Malliaras, *Nature* **2016**, 540, 379.
- [4] H. Sirringhaus, *Adv. Mater.* **2014**, 26, 1319.
- [5] M. Kaltenbrunner, T. Sekitani, J. Reeder, T. Yokota, K. Kuribara, T. Tokuhara, M. Drack, R. Schwödianer, I. Graz, S. Bauer-Gogonea, S. Bauer, T. Someya, *Nature* **2013**, 499, 458.
- [6] H. Kang, R. Kitsomboonloha, J. Jang, V. Subramanian, *Adv. Mater.* **2012**, 24, 3065.
- [7] T. Sekitani, T. Someya, *Mater. Today* **2011**, 14, 398.
- [8] A. de la Fuente Vornbrock, D. Sung, H. Kang, R. Kitsomboonloha, V. Subramanian, *Org. Electron.* **2010**, 11, 2037.
- [9] T. Sekitani, H. Nakajima, H. Maeda, T. Fukushima, T. Aida, K. Hata, T. Someya, *Nat. Mater.* **2009**, 8, 494.
- [10] T. Sekitani, M. Takamiya, Y. Noguchi, S. Nakano, Y. Kato, T. Sakurai, T. Someya, *Nat. Mater.* **2007**, 6, 413.
- [11] Y.-Y. Noh, N. Zhao, M. Caironi, H. Sirringhaus, *Nat. Nanotechnol.* **2007**, 2, 784.
- [12] J. B. Lee, V. Subramanian, *IEEE Trans. Electron Devices* **2005**, 52, 269.
- [13] G. Yu, J. Gao, J. C. Hummelen, F. Wudl, A. J. Heeger, *Science* **1995**, 270, 1789.
- [14] J. Youn, G. R. Dholakia, H. Huang, J. W. Hennek, A. Facchetti, T. J. Marks, *Adv. Funct. Mater.* **2012**, 22, 1856.
- [15] K. A. Singh, T. L. Nelson, J. A. Belot, T. M. Young, N. R. Dhumal, T. Kowalewski, R. D. McCullough, P. Nachimuthu, S. Thevuthasan, L. M. Porter, *ACS Appl. Mater. Interfaces* **2011**, 3, 2973.
- [16] Y.-Y. Noh, X. Cheng, M. Tello, M.-J. Lee, H. Sirringhaus, *Semicond. Sci. Technol.* **2011**, 26, 034003.
- [17] D. Boudinet, M. Benwadih, Y. Qi, S. Altazin, J.-M. Verilhac, M. Kroger, C. Serbutoviez, R. Gwoziecki, R. Coppard, G. Le Blevenec, A. Kahn, G. Horowitz, *Org. Electron.* **2010**, 11, 227.
- [18] X. Cheng, Y. Y. Noh, J. Wang, M. Tello, J. Frisch, R. P. Blum, A. Vollmer, J. P. Rabe, N. Koch, H. Sirringhaus, *Adv. Funct. Mater.* **2009**, 19, 2407.

- [19] P. Marmont, N. Battaglini, P. Lang, G. Horowitz, J. Hwang, A. Kahn, C. Amato, P. Calas, *Org. Electron.* **2008**, 9, 419.
- [20] D. He, J. Qiao, L. Zhang, J. Wang, T. Lan, J. Qian, Y. Li, Y. Shi, Y. Chai, W. Lan, L. K. Ono, Y. Qi, J.-B. Xu, W. Ji, X. Wang, *Sci. Adv.* **2017**, 3, e1701186.
- [21] C. G. Tang, M. C. Y. Ang, K.-K. Choo, V. Keerthi, J.-K. Tan, M. N. Syafiqah, T. Kugler, J. H. Burroughes, R.-Q. Png, L.-L. Chua, P. K. H. Ho, *Nature* **2016**, 539, 536.
- [22] S. Chung, M. Jang, S.-B. Ji, H. Im, N. Seong, J. Ha, S.-K. Kwon, Y.-H. Kim, H. Yang, Y. Hong, *Adv. Mater.* **2013**, 25, 4773.
- [23] Y. Zhou, C. Fuentes-Hernandez, J. Shim, J. Meyer, A. J. Giordano, H. Li, P. Winget, T. Papadopoulos, H. Cheun, J. Kim, M. Fenoll, A. Dindar, W. Haske, E. Najafabadi, T. M. Khan, H. Sojoudi, S. Barlow, S. Graham, J.-L. Brédas, S. R. Marder, A. Kahn, B. Kippelen, *Science* **2012**, 336, 327.
- [24] T. Minari, P. Darmawan, C. Liu, Y. Li, Y. Xu, K. Tsukagoshi, *Appl. Phys. Lett.* **2012**, 100, 093303.
- [25] M. Kröger, S. Hamwi, J. Meyer, T. Riedl, W. Kowalsky, A. Kahn, *Appl. Phys. Lett.* **2009**, 95, 123301.
- [26] M. Kano, T. Minari, K. Tsukagoshi, *Appl. Phys. Lett.* **2009**, 94, 143304.
- [27] S. Cho, J. H. Seo, K. Lee, A. J. Heeger, *Adv. Funct. Mater.* **2009**, 19, 1459.
- [28] B. H. Hamadani, D. J. Gundlach, I. McCulloch, M. Heeney, *Appl. Phys. Lett.* **2007**, 91, 243512.
- [29] D. J. Gundlach, L. Zhou, J. A. Nichols, T. N. Jackson, P. V. Necliudov, M. S. Shur, *J. Appl. Phys.* **2006**, 100, 024509.
- [30] S. Lee, G. Jo, S. J. Kang, G. Wang, M. Choe, W. Park, D. Y. Kim, Y. H. Kahng, T. Lee, *Adv. Mater.* **2011**, 23, 100.
- [31] Y. Xu, H. Sun, W. Li, Y.-F. Lin, F. Balestra, G. Ghibaudo, Y.-Y. Noh, *Adv. Mater.* **2017**, 29, 1702729.
- [32] Y. Xu, H. Sun, E.-Y. Shin, Y.-F. Lin, W. Li, Y.-Y. Noh, *Adv. Mater.* **2016**, 28, 8531.
- [33] B. Lüssem, C.-M. Keum, D. Kasemann, B. Naab, Z. Bao, K. Leo, *Chem. Rev.* **2016**, 116, 13714.
- [34] A. A. Günther, M. Sawatzki, P. Formánek, D. Kasemann, K. Leo, *Adv. Funct. Mater.* **2016**, 26, 768.

- [35] D. Khim, K.-J. Baeg, M. Caironi, C. Liu, Y. Xu, D.-Y. Kim, Y.-Y. Noh, *Adv. Funct. Mater.* **2014**, 24, 6252.
- [36] S. Singh, S. K. Mohapatra, A. Sharma, C. Fuentes-Hernandez, S. Barlow, S. R. Marder, B. Kippelen, *Appl. Phys. Lett.* **2013**, 102, 153303.
- [37] D. T. Duong, Y. Tuchman, P. Chakthranont, P. Cavassin, R. Colucci, T. F. Jaramillo, A. Salleo, G. C. Faria, *Adv. Electron. Mater.* **2018**, 4, 1800090.
- [38] S. N. Patel, A. M. Glaudell, K. A. Peterson, E. M. Thomas, K. A. O'Hara, E. Lim, M. L. Chabinyc, *Sci. Adv.* **2017**, 3, e1700434.
- [39] K. Kang, S. Watanabe, K. Broch, A. Sepe, A. Brown, I. Nasrallah, M. Nikolka, Z. Fei, M. Heeney, D. Matsumoto, K. Marumoto, H. Tanaka, S.-i. Kuroda, H. Sirringhaus, *Nat. Mater.* **2016**, 15, 896.
- [40] A. M. Glaudell, J. E. Cochran, S. N. Patel, M. L. Chabinyc, *Adv. Energy Mater.* **2015**, 5, 1401072.
- [41] J. E. Cochran, M. J. N. Junk, A. M. Glaudell, P. L. Miller, J. S. Cowart, M. F. Toney, C. J. Hawker, B. F. Chmelka, M. L. Chabinyc, *Macromolecules* **2014**, 47, 6836.
- [42] J. Li, C. W. Rochester, I. E. Jacobs, S. Friedrich, P. Stroeve, M. Riede, A. J. Moulé, *ACS Appl. Mater. Interfaces* **2015**, 7, 28420.
- [43] A. Dai, A. Wan, C. Magee, Y. Zhang, S. Barlow, S. R. Marder, A. Kahn, *Org. Electron.* **2015**, 23, 151.
- [44] B. Lüssem, M. Riede, K. Leo, *phys. status solidi A* **2013**, 210, 9.
- [45] I. Bruder, S. Watanabe, J. Qu, I. B. Müller, R. Kopecek, J. Hwang, J. Weis, N. Langer, *Org. Electron.* **2010**, 11, 589.
- [46] W. Gao, A. Kahn, *Org. Electron.* **2002**, 3, 53.
- [47] W. Gao, A. Kahn, *Appl. Phys. Lett.* **2001**, 79, 4040.
- [48] T. Umeda, S. Tokito, D. Kumaki, *J. Appl. Phys.* **2007**, 101, 054517.
- [49] S. Himmelberger, J. Dacuña, J. Rivnay, L. H. Jimison, T. McCarthy-Ward, M. Heeney, I. McCulloch, M. F. Toney, A. Salleo, *Adv. Funct. Mater.* **2013**, 23, 2091.
- [50] C. Wang, L. H. Jimison, L. Goris, I. McCulloch, M. Heeney, A. Ziegler, A. Salleo, *Adv. Mater.* **2010**, 22, 697.
- [51] I. McCulloch, M. Heeney, C. Bailey, K. Genevicius, I. MacDonald, M. Shkunov, D. Sparrowe, S. Tierney, R. Wagner, W. Zhang, M. L. Chabinyc, R. J. Kline, M. D. McGehee, M. F. Toney, *Nat. Mater.* **2006**, 5, 328.

- [52] K. Cho, J. Pak, J.-K. Kim, K. Kang, T.-Y. Kim, J. Shin, B. Y. Choi, S. Chung, T. Lee, *Adv. Mater.* **2018**, 30, 1705540.
- [53] J.-K. Kim, Y. Song, T.-Y. Kim, K. Cho, J. Pak, B. Y. Choi, J. Shin, S. Chung, T. Lee, *Nanotechnology* **2017**, 28, 47LT01.
- [54] Y. Xu, T. Minari, K. Tsukagoshi, J. A. Chroboczek, G. Ghibaudo, *J. Appl. Phys.* **2010**, 107, 114507.
- [55] M. C. Gwinner, R. D. Pietro, Y. Vaynzof, K. J. Greenberg, P. K. H. Ho, R. H. Friend, H. Sirringhaus, *Adv. Funct. Mater.* **2011**, 21, 1432.
- [56] N. Zhao, Y. Y. Noh, J. F. Chang, M. Heaney, I. McCulloch, H. Sirringhaus, *Adv. Mater.* **2009**, 21, 3759.
- [57] T. Umeda, D. Kumaki, S. Tokito, *J. Appl. Phys.* **2009**, 105, 024516.
- [58] P. Reiser, L. Müller, V. Sivanesan, R. Lovrincic, S. Barlow, S. R. Marder, A. Pucci, W. Jaegermann, E. Mankel, S. Beck, *J. Phys. Chem. C* **2018**, 122, 14518.
- [59] J. Li, C. Koshnick, S. O. Diallo, S. Ackling, D. M. Huang, I. E. Jacobs, T. F. Harrelson, K. Hong, G. Zhang, J. Beckett, M. Mascal, A. J. Moulé, *Macromolecules* **2017**, 50, 5476.
- [60] P. A. Stolk, H. J. Gossman, D. J. Eaglesham, D. C. Jacobson, C. S. Rafferty, G. H. Gilmer, M. Jaraíz, J. M. Poate, H. S. Luftman, T. E. Haynes, *J. Appl. Phys.* **1997**, 81, 6031.
- [61] P. M. Fahey, P. B. Griffin, J. D. Plummer, *Rev. Mod. Phys.* **1989**, 61, 289.
- [62] I. Salzmann, G. Heimel, M. Oehzelt, S. Winkler, N. Koch, *Acc. Chem. Res.* **2016**, 49, 370.
- [63] P. Pingel, D. Neher, *Phys. Rev. B* **2013**, 87, 115209.
- [64] M. L. Tietze, J. Benduhn, P. Pahner, B. Nell, M. Schwarze, H. Kleemann, M. Krammer, K. Zojer, K. Vandewal, K. Leo, *Nat. Commun.* **2018**, 9, 1182.
- [65] A. J. Kronemeijer, V. Pecunia, D. Venkateshvaran, M. Nikolka, A. Sadhanala, J. Moriarty, M. Szumilo, H. Sirringhaus, *Adv. Mater.* **2014**, 26, 728.
- [66] M. Fahlman, A. Crispin, X. Crispin, S. K. M. Henze, M. P. de Jong, W. Osikowicz, C. Tengstedt, W. R. Salaneck, *J. Phys. Condens. Matter* **2007**, 19, 183202.
- [67] W. Osikowicz, M. P. de Jong, S. Braun, C. Tengstedt, M. Fahlman, W. R. Salaneck, *Appl. Phys. Lett.* **2006**, 88, 193504.

- [68] S. Olthof, W. Tress, R. Meerheim, B. Lüssem, K. Leo, *J. Appl. Phys.* **2009**, 106, 103711.
- [69] M. Leskelä, M. Ritala, *Thin Solid Films* **2002**, 409, 138.
- [70] M. J. Lee, D. Gupta, N. Zhao, M. Heeney, I. McCulloch, H. Sirringhaus, *Adv. Funct. Mater.* **2011**, 21, 932.
- [71] Y. Wu, B. Lee, H.-S. P. Wong, *IEEE Electron Device Lett.* **2010**, 31, 1449.

# **Chapter 3. Highly stable contact doping in organic field effect transistors by dopant-blockade method**

*In organic device applications, downscaling and high-speed operation are essential, and a high contact resistance between metal electrodes and organic semiconductors fundamentally limits the device performance. Recently, various contact doping methods have been reported as an effective way to resolve the contact resistance problem. However, the contact doping has not been explored extensively in organic field effect transistors (OFETs) due to dopant diffusion problem which significantly degrades the device stability by damaging the ON/OFF switching performance. Here, I improved the stability of a contact doping method by incorporating “dopant-blockade molecules” in poly(2,5-bis(3-hexadecylthiophen-2-yl)thieno [3,2-b]thiophene) (PBTTT) film in order to suppress the diffusion of the dopant molecules. By carefully selecting the dopant-blockade molecules for effectively blocking the dopant diffusion paths, the ON/OFF ratio of PBTTT OFETs could be maintained over two months. This work would maximize the potential of OFETs by employing the contact doping method as a promising route towards resolving the contact resistance problem.*

## **3.1. Introduction**

Developing high-performance organic field effect transistors (OFETs) has been a bottleneck in exploiting the merits of organic semiconductors (OSCs) such as solution-processability, mechanical flexibility and bio-compatibility, for realizing practical organic optoelectronic device applications.<sup>[1-12]</sup> In particular, considering the industrial success of organic light emitting diodes (OLEDs), OFETs could be potentially used as switching and driving transistors in the organic flexible display panels.<sup>[13-14]</sup> To meet future technological

demands, downscaling and high-speed operation of OFETs are necessary. However, a high contact resistance between metal electrodes and OSCs remains as one of the dominant obstacles for utilizing OFETs because the high contact resistance decreases the effective mobility of OFETs and limits the range of the operation voltage for achieving high-frequency operation as a switching transistor.<sup>[15-17]</sup>

To overcome the contact resistance problem in OFETs, there have been a diverse range of approaches including self-assembled monolayer (SAM) treatment on metal electrodes by organic molecules<sup>[18-24]</sup> and introducing charge injection layer between metal electrodes and OSCs.<sup>[25-31]</sup> In addition, contact doping (i.e. introduction of external molecules near contact regions) has been studied as an effective method for improving contact properties.<sup>[32-35]</sup> An ideal contact doping technique in OFETs would meet two criteria; firstly, a high maximum doping level for enhancing charge injection and secondly a spatial confinement of dopants for device stability. However, these two requirements cannot often be simultaneously achieved since achieving a high doping level requires a large dopant density, which leads to a faster diffusion of dopant molecules within the host semiconductor. This dopant diffusion problem results in a rise of the OFF current due to an unintentional doping of the active channel. Confining the dopant molecules within the selective regions near the contacts is especially challenging in the case of bulk-doping since a large concentration gradient of dopant density at the edges of the doped regions accelerates the dopant diffusion. The dopants from the contact regions diffuse towards the active channel region which should remain un-doped in order to maintain a sharp ON/OFF switching characteristic in OFETs. Therefore, the dopant diffusion has limited the contact doping techniques to be employed extensively in OFETs.

Despite a significant level of attention given in the dopant diffusion problem in



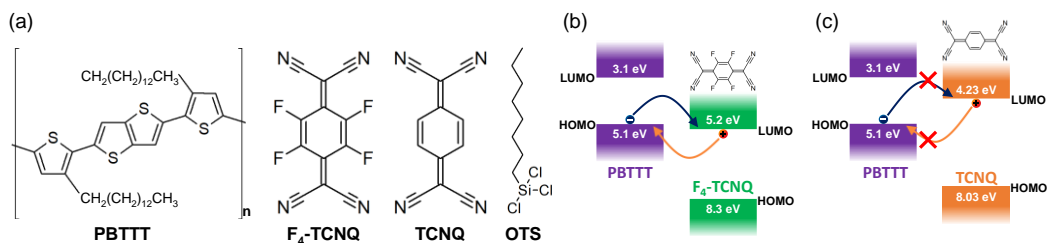
organic solar cells and OLEDs,<sup>[36-43]</sup> there have been relatively few studies which have focused on OFETs. Recently, I have developed a surface etching treatment for suppressing the dopant diffusion in doped-contact poly(2,5-bis(3-tetradecylthiophen-2-yl)thieno[3,2-b]thiophene) (PBTTT) OFETs.<sup>[44]</sup> This system exploited a facile and efficient bulk-doping of PBTTT via solid-state diffusion of 2,3,5,6-tetrafluoro-7,7,8,8-tetracyanoquinodimethane (F<sub>4</sub>-TCNQ) which resulted in a high-conductivity and high carrier-concentration regions in spatially selected regions in OFETs.<sup>[45]</sup> This doping method effectively reduced the contact resistance (by a factor of 5) and showed its potential by demonstrating the low-voltage operation organic transistor. However, despite an improved device stability by the surface etching treatment, suppressing the diffusion of dopant molecules from the contact regions to the channel region of PBTTT OFETs could not be completely avoided, and thereby resulting in degradation of the switching characteristics of OFETs.

In this study, the stability of the contact doping method in PBTTT OFETs was significantly improved by introducing a novel technique for suppressing the dopant diffusion. The diffusion pathways of the dopants within the active channel region were spatially blocked by incorporating tetracyanoquinodimethane (TCNQ) as “dopant-blockade molecules” in PBTTT OFETs. The dopant-blockade molecules were carefully chosen such that they are electrically inactive and they readily locate themselves in the diffusion paths of the dopants. This technique effectively constructed barriers against the motion of dopant molecules by incorporating the dopant-blockade molecules. This concept can be considered analogous to a recent work which achieved a high operational and environmental stability by filling voids that can act as water adsorption sites in the polymer film of OFETs by using a specific range of organic solvents and molecules.<sup>[46]</sup> In this work,

I demonstrated that introducing TCNQ as dopant-blockade molecules in PBTTT film remarkably increase the device stability against dopant diffusion by comparing the OFETs with and without the TCNQ incorporation.

## 3.2. Experiments

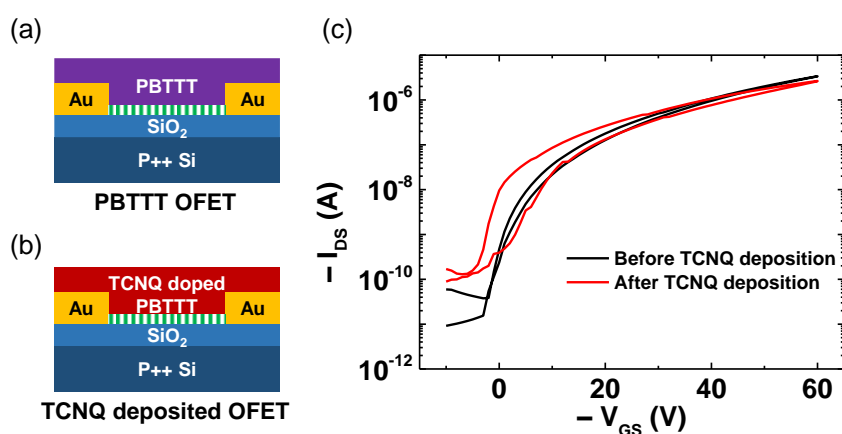
### 3.2.1. Materials and device fabrication process



**Figure 3.1** (a) Molecular structures of PBTTT, F<sub>4</sub>-TCNQ, TCNQ and OTS. (b) HOMO and LUMO levels of PBTTT and F<sub>4</sub>-TCNQ. (c) HOMO and LUMO levels of PBTTT and TCNQ.

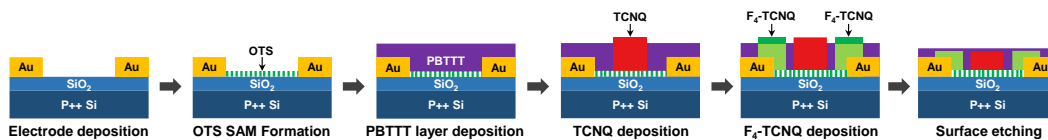
Figure 3.1a shows the molecular structures of the organic materials used in this work. In order to suppress the dopant diffusion in the channel region of the PBTTT OFETs, I adopted dopant-blockade molecules in the F<sub>4</sub>-TCNQ-doped-contact PBTTT OFETs which are fabricated in the same way as the previous chapter.<sup>[44]</sup> The dopant-blockade molecules should be selected to avoid the charge transfer reaction with PBTTT molecules for maintaining the electrical properties of the doped-contact PBTTT OFETs (denoted as “DC-FET”) after introducing dopant-blockade molecules in the PBTTT channel. Figure 3.1b and c show the values of the highest occupied molecular orbital (HOMO) level and lowest unoccupied molecular orbital (LUMO) level of F<sub>4</sub>-TCNQ and TCNQ. TCNQ was adopted as the dopant-blockade molecule because it has a similar molecular structure with F<sub>4</sub>-TCNQ but the LUMO level is higher than the HOMO level of PBTTT which energetically prohibits the charge transfer reaction with PBTTT.<sup>[47]</sup> On the contrary, the charge transfer reaction between PBTTT and F<sub>4</sub>-TCNQ is energetically favorable because the HOMO level of PBTTT is higher than the LUMO level of F<sub>4</sub>-TCNQ. Therefore,

electrons transfer easily from PBTTT to F<sub>4</sub>-TCNQ, whereas the charge transfer between PBTTT and TCNQ is energetically unfavorable. Based on this energetic mismatch between the HOMO level of PBTTT and LUMO level of TCNQ, it was expected that introducing TCNQ molecules in the channel region hardly affects the electrical properties of PBTTT films. To verify this idea, I compared the pristine PBTTT OFET and the PBTTT OFET with TCNQ molecules deposited on the entire PBTTT channel.



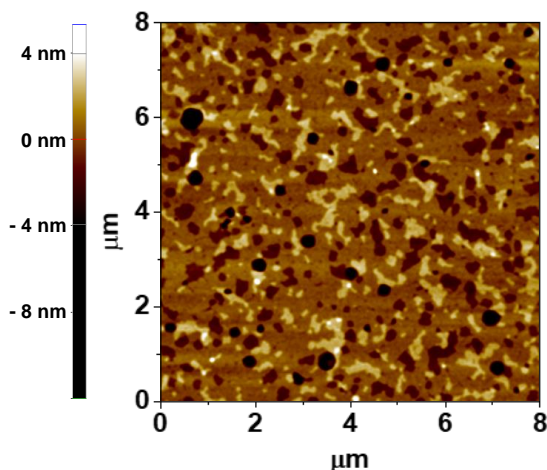
**Figure 3.2** Schematic images of (a) the PBTTT OFET and (b) the PBTTT OFET with TCNQ molecules deposited on the entire PBTTT channel. (c) The transfer curves of the PBTTT OFET (black line) and PBTTT OFET with TCNQ molecules deposited on the entire PBTTT channel (red line).

As the electrical results in Figure 3.2c, the transistor characteristics of the PBTTT OFETs was well preserved, compared to the entire-doped PBTTT OFET with F<sub>4</sub>-TCNQ which became a conductor rather than a transistor due to doping.<sup>[44]</sup>



**Figure 3.3** Schematic images of the fabrication process of the dopant-blockade PBTTT OFET. The red regions in the middle of transistors is the TCNQ-incorporated regions. The dark green regions represent the neutral F<sub>4</sub>-TCNQ molecules which are not involved in the charge transfer reaction with PBTTT molecules. The bright green regions are the doped-PBTTT regions by using F<sub>4</sub>-TCNQ dopant molecules.

Figure 3.3 shows how the TCNQ molecules were incorporated in the doped-contact PBTTT FETs by entailing the step-by-step fabrication process of the TCNQ-incorporated doped-contact PBTTT OFET (dopant-blockaded doped-contact-FET, denoted as “DB/DC-FET”). First, SiO<sub>2</sub>/Si substrates were cleaned by sonication with de-ionized water, isopropanol and acetone for 10 min in each cleaning solvent. Ti/Au (2 nm/30 nm) electrodes were deposited on the cleaned substrates as source and drain electrodes by using an electron-beam evaporator under 10<sup>-6</sup> torr, patterned by shadow masks. 30 mM octyltrichlorosilane (OTS) solution was prepared by dissolving OTS in toluene solvent. The substrates were then transferred to N<sub>2</sub> filled glove box and immersed in the OTS solution over 12 hours to form the OTS self-assembled monolayer on SiO<sub>2</sub> surfaces. The OTS-treated substrates were cleaned again by isopropanol, acetone and toluene for 10 min in each solvent with sonication to remove residual OTS molecules on the surface. Poly(2,5-bis(3-hexadecylthiophen-2-yl)thieno [3,2-b]thiophene) (PBTTT) solution was made by dissolving PBTTT in 1,2-dichlorobenzene with the concentration of 9 mg/mL and heated at 110 °C before the spin-coating. Then, the PBTTT solution was spin-coated on the OTS-treated substrates with 1500 rpm for 45 s. After that, the PBTTT deposited substrates were



**Figure 3.4** The surface morphology of the PBTTT film deposited on the OTS-treated SiO<sub>2</sub>/Si substrate measured by atomic force microscope.

annealed at 180 °C for 20 min and cooled down slowly to form a clear terrace morphology as a result in Figure 3.4.<sup>[48-51]</sup>

After that, TCNQ molecules were selectively incorporated in the middle of the channel region of the PBTTT transistor with the nominal thickness of 10 nm by using a thermal evaporator under  $5 \times 10^{-6}$  torr with a shadow mask. Then, F<sub>4</sub>-TCNQ molecules were deposited near the metal contact regions of the device with the nominal thickness of 10 nm by the same method for TCNQ deposition. The thermal evaporation method used for both the TCNQ and F<sub>4</sub>-TCNQ deposition ensures the spatial selectivity, i.e. the position of the dopant-blockade molecules (TCNQ) are limited in the conduction channel region of OFETs, separated from the contact regions near the source and drain electrodes. The shadow mask for patterning the F<sub>4</sub>-TCNQ molecules was carefully aligned under an optical microscope in order to avoid the spatial overlap between the F<sub>4</sub>-TCNQ-doped region and TCNQ-incorporated region. This is important since the presence of the TCNQ molecules near the contact regions could interrupt the charge transfer between the dopant molecules (F<sub>4</sub>-TCNQ) and the host PBTTT molecules, and therefore resulting in a lower doping efficiency.

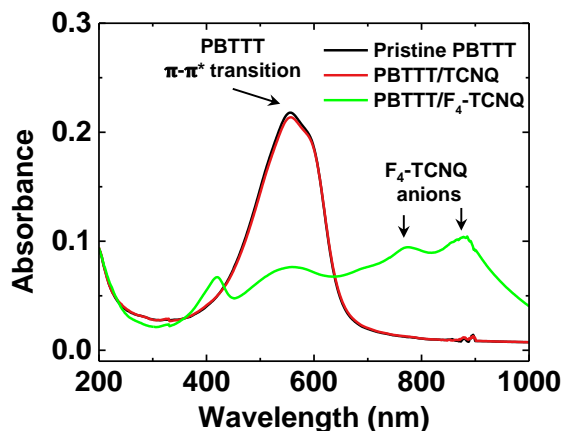
Finally, the devices were etch-treated by argon plasma (50 W, 1 s) for further enhancing the device stability by removing the neutral F<sub>4</sub>-TCNQ molecules which are highly diffusive compared to their charged counterparts.<sup>[44,52-53]</sup> The samples for UV-Vis absorption, ToF-SIMS and XRR measurements were prepared in the same way as above without the patterning on the different substrates; fused silica windows for UV-Vis absorption measurement and bare Si substrates for ToF-SIMS and XRR measurements.

### **3.2.2. Device and film characterization**

Electrical measurement was performed by a semiconductor parameter analyzer (Keithley 4200 SCS) under vacuum condition ( $\sim 10^{-3}$  torr). Ultraviolet-visible (UV-Vis) absorptions were measured by UV/Vis spectroscopy (JASCO V-770). Element depth profiles were acquired by a time-of-flight secondary ion mass spectrometry (ToF.SIMS<sup>5</sup>, Iontof). XRR scans were measured on a home diffractometer (3303TT, GE) using Cu K $\alpha$ -radiation ( $\lambda = 1.5406 \text{ \AA}$ ) and a 1D detector (Meteor 1D, XRD Eigenmann) (work in collaboration with Prof. K. Broch in university of Tübingen).

### 3.3. Results & Discussions

#### 3.3.1. Ultraviolet-visible absorption spectroscopy



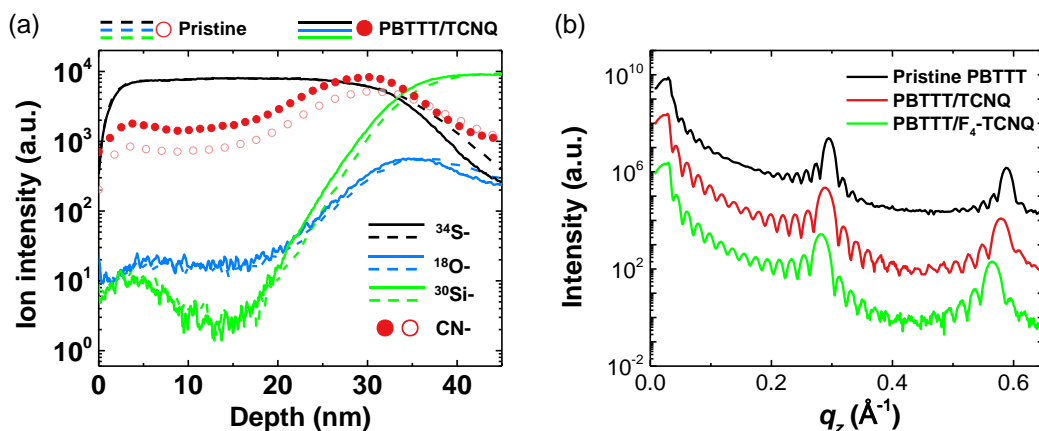
**Figure 3.5** UV-Vis spectroscopy data for the pristine PBTBT film (black line), PBTBT/TCNQ film (red line) and PBTBT/ $F_4$ -TCNQ film.

The absence of the charge transfer reaction between TCNQ and PBTBT was confirmed by ultraviolet-visible (UV-Vis) absorption spectroscopy measurements. Figure 3.5 displays the UV-Vis absorption data of a pristine PBTBT film (black line), a TCNQ-incorporated PBTBT film (PBTBT/TCNQ, shown as a red line) and a  $F_4$ -TCNQ-doped PBTBT film (PBTBT/ $F_4$ -TCNQ, shown as a green line). The pristine PBTBT film (black line) showed a clear  $\pi$ - $\pi^*$  transition peak near 550 nm.<sup>[44-45]</sup> On the other hand, the PBTBT/ $F_4$ -TCNQ film (green line) displayed a clear bleaching of a PBTBT  $\pi$ - $\pi^*$  transition peak. In addition, the  $F_4$ -TCNQ anion peaks near 800 nm and 900 nm appeared and a broad polaron absorption of charged PBTBT was observed from 600 nm to 1000 nm. These changes of the absorption spectrum were caused by the charge transfer between PBTBT and  $F_4$ -TCNQ.<sup>[44]</sup> However, for the PBTBT/TCNQ film (red line), the absorption data almost unchanged, compared with the pristine film. This good agreement between the



pristine film and PBTTT/TCNQ film supported the absence of the charge transfer reaction between PBTTT and TCNQ.

### 3.3.2. ToF-SIMS and XRR measurements



**Figure 3.6** (a) The depth profiles of ion intensity for the pristine PBTTT film (dashed lines and empty symbols) and PBTTT/TCNQ film (solid lines and filled symbols); the sulfur ion signals are black solid and dashed lines, the oxygen ion blue solid and dashed lines, silicon ion green solid and dashed lines and the cyanide ion signal red empty and filled circle symbols. (b) The XRR data of the pristine PBTTT film (black line), the PBTTT/TCNQ film (red line) and the PBTTT/ $\text{F}_4$ -TCNQ film (green line). The intervals between large  $q_z$  peaks of each film represent the out-of-plane lamellar stacking distance.

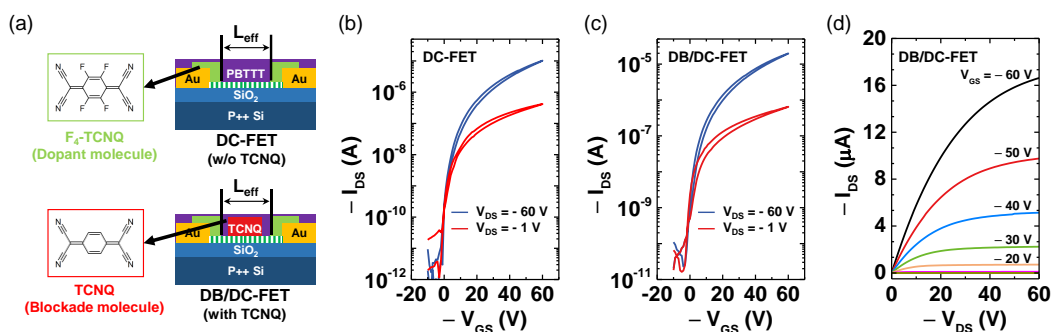
In order to effectively block the diffusion paths of the dopant molecules, the dopant blockade molecules would ideally be bulk-incorporated in the PBTTT film. Considering that  $\text{F}_4$ -TCNQ undergoes solid-state diffusion by penetrating all the way down to the substrate from the top surface of the PBTTT films, it was expected that TCNQ would also undergo solid-state diffusion in PBTTT due to a similar molecular structure. Figure 3.6a shows elemental depth profiles of the pristine PBTTT film (dashed lines and empty symbols) and the PBTTT/TCNQ film (solid lines and filled symbols) by time of flight

secondary ion mass spectroscope (ToF-SIMS). The sulfur ion signal ( $^{34}\text{S}$ -, black solid and dashed lines) is a representative signal of PBTTT, both the oxygen ion ( $^{18}\text{O}$ -, blue solid and dashed lines) and silicon ion ( $^{30}\text{Si}$ -, green solid and dashed lines) signals for the silicon substrates and the cyanide ion signal ( $\text{CN}$ -, red empty and filled circle symbols) for TCNQ. The increases in the depth profiles of the cyanide ion intensity shown at each interface between two different media (i.e. vacuum/PBTTT and PBTTT/ $\text{SiO}_2$  interfaces) could be related to the matrix effect.<sup>[54-56]</sup> Comparing the pristine PBTTT film and PBTTT/TCNQ film, the sulfur, oxygen and silicon ions signals showed very similar depth profiles due to the same constituents of the both samples from PBTTT and silicon substrates. On the contrary, the PBTTT/TCNQ film showed a higher cyanide ion signal than the pristine PBTTT film down to the depth of nearly 40 nm which is the thickness of the PBTTT film.<sup>[45]</sup> Therefore, the depth profile of the elemental analysis indicates that TCNQ molecules become structurally incorporated in PBTTT films all the way down to the interface between the PBTTT film and the silicon substrate by solid-state diffusion.

Figure 3.6b shows the x-ray reflectivity (XRR) data of the pristine PBTTT film (black line), the PBTTT/TCNQ film (red line) and the PBTTT/ $\text{F}_4$ -TCNQ film (green line). The previous chapter showed that  $\text{F}_4$ -TCNQ molecules were located at the side chain regions in the PBTTT film when  $\text{F}_4$ -TCNQ molecules were deposited on a PBTTT polymer film.<sup>[45, 57-59]</sup> Upon the molecular intercalation of  $\text{F}_4$ -TCNQ, the out-of-plane lamellar stacking distance of the PBTTT/ $\text{F}_4$ -TCNQ film becomes larger than that of the pristine PBTTT film. The expansion of the out-of-plane lamellar stacking distance after  $\text{F}_4$ -TCNQ doping was indicated by a shorter  $q_z$  spacing between the ( $h00$ ) diffraction peaks of the PBTTT/ $\text{F}_4$ -TCNQ film compared to that of the pristine film. If the TCNQ molecules are located at the side chain space in a PBTTT film by solid-state diffusion, the deposition of

TCNQ molecules would also cause the expansion of the out-of-plane lamellar stacking distance in the PBTTT/TCNQ film. Compared with the pristine film, the smaller  $q_z$  spacing between ( $h00$ ) diffraction peaks of the PBTTT/TCNQ film indicates the expansion of the out-of-plane lamellar stacking distance due to the presence of the TCNQ molecules in the side chain space of PBTTT film. The extracted out-of-plane lamellar spacing was 21.64 Å for the PBTTT/TCNQ film and 21.37 Å for the pristine PBTTT film. The expansion of the lamellar spacing was even larger for the PBTTT/ $F_4$ -TCNQ film for which the extracted value was 22.21 Å. The larger expansion in the lamellar spacing of the PBTTT/ $F_4$ -TCNQ film could be correlated with the bigger size of  $F_4$ -TCNQ molecules relative to TCNQ molecules. Based on the results of the UV-Vis absorption, ToF-SIMS and XRR measurements, I deduced that TCNQ molecules diffused into the bulk of PBTTT film by the solid-state diffusion all the way down to the bottom substrate, without a significant charge transfer reaction with PBTTT molecules.

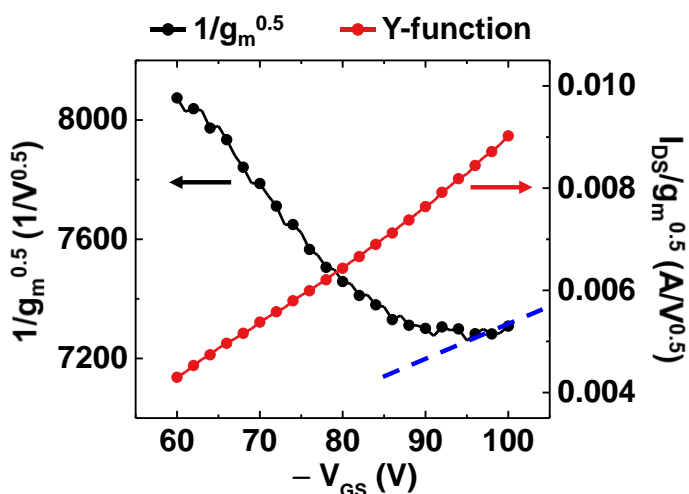
### 3.3.3. Electrical characterization of the DB/DC-FET



**Figure 3.7** (a) Schematic images of the DC-FET (w/o TCNQ) and DB/DC-FET (with TCNQ). The transfer curves of (b) the DC-FET and (c) the DB/DC-FET. (d) The output curves of the DB/DC-FET.

Figure 3.7a shows the schematic images of the DC-FET (w/o TCNQ) and the DB/DC-FET (with TCNQ). Figure 3.7b and c show the transfer curves of the doped-contact PBTTT OFET (DC-FET) and TCNQ-incorporated doped-contact PBTTT OFET (DB/DC-FET) in linear (red line) and saturation (blue line) regimes. Transfer curves of the both devices show similar electrical characteristics. The DB/DC-FET showed typical p-type OFET device characteristics with the mobility of  $0.058 \text{ cm}^2/\text{V}\cdot\text{s}$ . Figure 3.7d shows the output curves of the  $50 \text{ }\mu\text{m}$  channel length DB/DC-FET. The device shows a clear ohmic behavior in a low  $V_{DS}$  region, providing evidence of a low contact resistance. To extract the contact resistance of the DB/DC-FET, I used Y-function method as the same way in the previous chapter.

Figure 3.8 displays the data for the Y-function method; a black line shows  $1/\sqrt{g_m}$  (where  $g_m$  is the transconductance) and a red line is the Y-function. The extracted contact resistance of the DB/DC-FET was  $4.55 \text{ k}\Omega\cdot\text{cm}$  which is comparable to the previous result for the DC-FET. Despite of the additional incorporation of TCNQ molecules in the

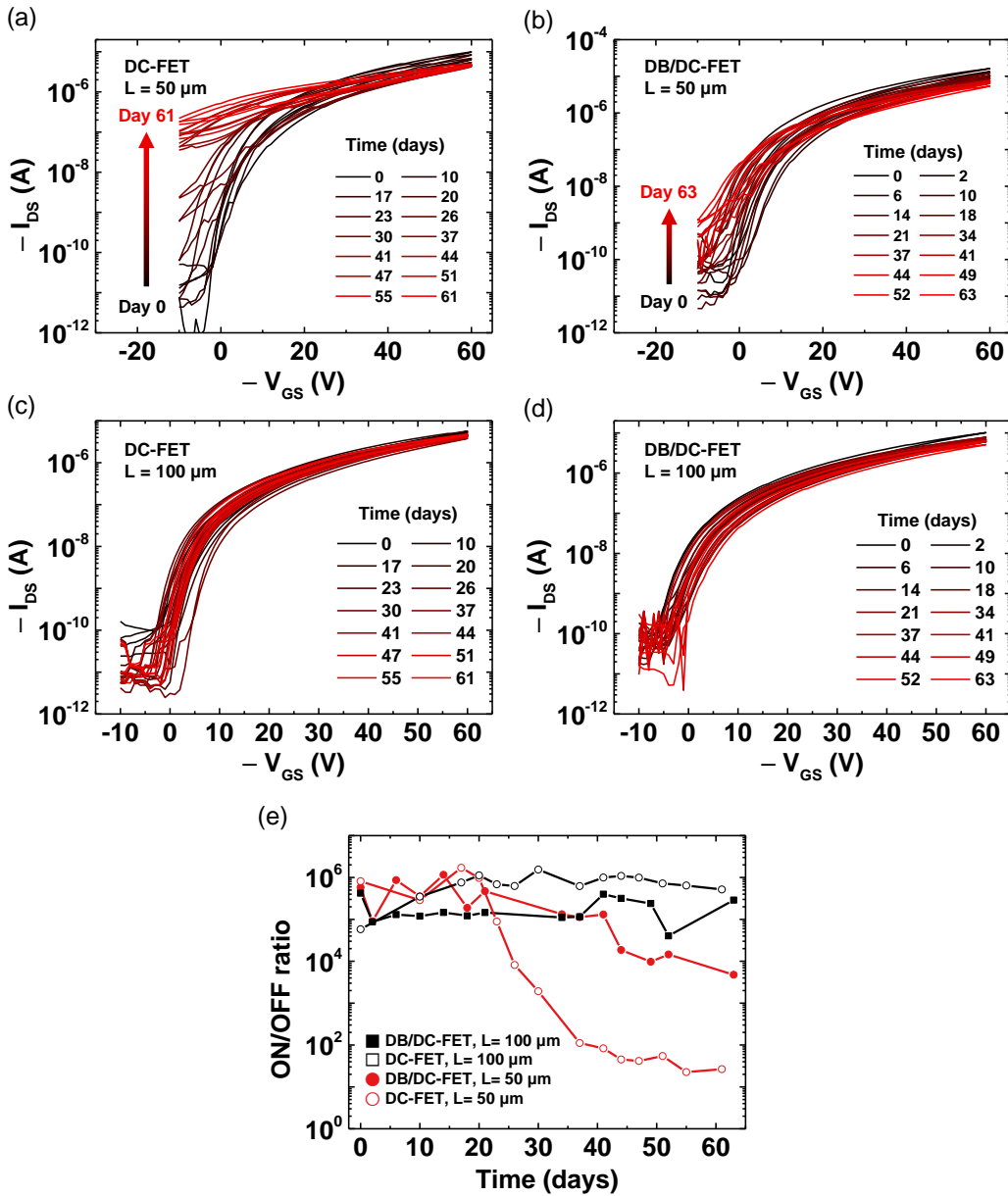


**Figure 3.8** Data for Y-function method; a black line shows  $1/\sqrt{g_m}$  (where  $g_m$  is the transconductance), a red line is the Y-function and a blue dashed line represents the selected data to extract contact resistance.

PBTTT channel before the contact doping with F<sub>4</sub>-TCNQ molecules, the contact doping remained effective for achieving a low contact resistance; the pristine PBTTT OFET had more than 5 times larger contact resistance value of 24.5 kΩ•cm.<sup>[44]</sup> Therefore, I deduced that the incorporation of the dopant-blockade molecules did not affect the operation properties of the DC-FET.

### 3.3.4. ON/OFF ratio stability of the DB/DC-FET

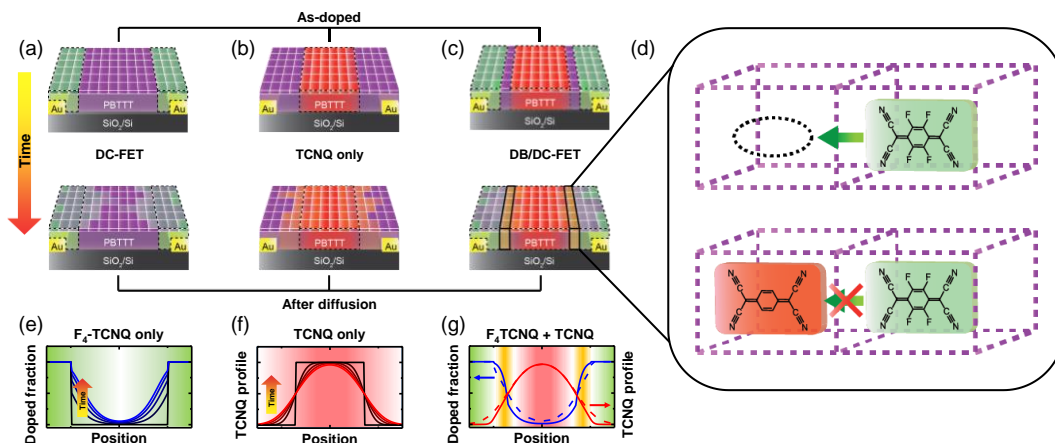
Figure 3.9a to d show the change of the transfer curves of the DC-FET and the DB/DC-FET with the channel length of 50 μm and 100 μm, respectively, over two months. From Figure 3.9a, it is clear that the ON/OFF ratio of the DC-FET decreases due to the rise of the OFF current. On the other hand, the rise of the OFF current of the DB/DC-FET is significantly less, which is presented in Figure 3.9b. Figure 3.9e shows the traces of the ON/OFF ratio of the both kinds of the devices for two months; the DC-FET is denoted as empty symbols, the DB/DC-FET as filled symbols, 100 μm channel length devices as black lines and 50 μm channel length devices as red lines. For 100 μm channel devices, the traces of the both kinds of devices had stable ON/OFF ratio greater than 10<sup>4</sup> over the two months. The stability of the ON/OFF ratio of the 100 μm channel length devices reproduces the previous results for the DC-FET.<sup>[44]</sup> On the contrary, for the 50 μm channel length devices, the ON/OFF ratio stability was affected significantly by the TCNQ incorporation. The trace of the DC-FET decreases steeply from 20 days to 40 days. However, the trace of the DB/DC-FET shows the ON/OFF ratio decaying much slower and the ON/OFF ratio remained higher than 10<sup>3</sup> for two months. Therefore, based on these traces of the ON/OFF ratio of devices, I have found that the dopant-blockade method is effective for achieving stable DC-FETs.



**Figure 3.9** Time evolution of the transfer curves for (a) the DC-FET with the channel length,  $L_{ch}$ , of  $50 \mu\text{m}$ , (b) the DB/DC-FET with  $L_{ch} = 50 \mu\text{m}$ , (c) the DC-FET with  $L_{ch} = 100 \mu\text{m}$  and (d) the DB/DC-FET with  $L_{ch} = 100 \mu\text{m}$  over two months. (e) The ON/OFF ratio of the DC-FET and the DB/DC-FET over time with the channel length of  $50 \mu\text{m}$  and  $100 \mu\text{m}$ .

In order to describe the dopant-blockade effect on the dopant diffusion in details, I first considered the diffusion of the dopant and dopant-blockade molecules independently within PBTTT OFETs. Figure 3.10a and b illustrate the propagation of the dopant molecules within the channel regions of the DC-FET and that of the dopant-blockade molecules in the TCNQ-incorporated PBTTT OFET (denoted as “TCNQ only”), respectively. Figure 3.10a describes the expansion of the doped PBTTT regions; purple regions represent neutral PBTTT regions, green for doped PBTTT regions, darker green for higher dopant concentration, and black dashed lines define the initially doped regions by F<sub>4</sub>-TCNQ molecules (Figure 3.10a, above). As time passes, the doped regions expand by the diffusion of dopant molecules into the channel and create conduction paths between the two electrodes (Figure 3.10a, bottom), and therefore the OFF current increases. Figure 3.10b depicts the diffusion of TCNQ molecules in the channel region of “TCNQ only” device. The red regions represent the TCNQ molecules in the PBTTT channel, more vivid red for higher TCNQ concentration. The TCNQ molecules are initially confined in the middle of the channel (Figure 3.10b, above) as described in the fabrication process (Figure 3.3), which is denoted as black dashed lines. The TCNQ molecules diffuse towards the contact regions from the middle of the channel along the concentration gradient as time passes (Figure 3.10b, bottom).

In DB/DC-FETs, both the F<sub>4</sub>-TCNQ molecules (dopant) and TCNQ molecules (dopant-blockade) diffuse together in the opposite directions, affecting the motion of each other, as shown in Figure 3.10c. The orange regions (Figure 3.10c, bottom) represent the channel regions where the dopant and dopant-blockade molecules co-exist and both molecules hinder the diffusion of one another by occupying the potential diffusion sites in the PBTTT film. This process is depicted in Figure 3.10d. If there was no TCNQ dopant-



**Figure 3.10** Schematic diagrams of (a) the propagation of doped regions in the DC-FET, (b) the diffusion of TCNQ molecules in the channel region of the TCNQ-incorporated PBTTT OFET and (c) the diffusion of  $F_4$ -TCNQ and TCNQ molecules in the opposite directions for the DB/DC-FET. (d) The illustration for hindrance by the dopant-blockade molecules against the diffusion of the dopant molecules in the void spaces of the PBTTT film. (e) The predicted profiles of the doped fraction of PBTTT molecules at different positions of the channel in the DC-FET. (f) The spatial diffusion profile of TCNQ molecules in the PBTTT channel of the TCNQ-incorporated PBTTT OFET. (g) The predicted changes in the profiles of the doped fraction of PBTTT molecules and the spatial diffusion of TCNQ molecules for the DB/DC-FET as blue and red solid lines. Dashed lines taken from Figure 3.10e and f for comparison.

blockade molecule, the dopant molecules move easily into the neighboring empty site. However, if a dopant-blockade molecule already occupies the neighboring empty site, the dopant molecule is sterically hindered from moving to the next site.

The effect of the dopant-blockade molecules on the dopant diffusion can be summarized by Figure 3.10e, f and g which show the predicted molecular diffusion profile for the different kinds of devices. Figure 3.10e shows the doped fraction of PBTTT molecules at different positions of the channel in the DC-FET without the dopant-blockade molecules (“ $F_4$ -TCNQ only”). As time passes, the doped fraction at the center of the



channel increases gradually, which induces the rise of the OFF current in the DC-FET. The black line is the initial doped fraction of PBTTT molecules for the as-prepared DC-FET and the time evolution of the doped fraction of PBTTT molecules predicted by the same numerical simulation method used in the previous chapter is indicated by an arrow.<sup>[44]</sup> Figure 3.10f shows a spatial diffusion profile of TCNQ molecules in the “TCNQ-only” device. I predicted that the diffusion of TCNQ molecules followed one-dimensional Fick’s diffusion equation without any correction terms (unlike F<sub>4</sub>-TCNQ), considering that TCNQ molecules undergo diffusion in the PBTTT film without electrostatic attraction with PBTTT molecules due to the lack of charge transfer reaction. Figure 3.10g shows predicted changes in the previous two graphs for the DB/DC-FET (“F<sub>4</sub>-TCNQ + TCNQ”). The doped fraction of PBTTT molecules and the TCNQ molecule distribution in the PBTTT channel are shown as blue lines and red lines respectively; solid line for the DB/DC-FET and dashed line taken from Figure 3.10e and 3.10f for comparison. The reduction of the doped fraction of PBTTT molecules in the middle of the channel is clearly shown from Figure 3.10g for which I assumed that the diffusion of F<sub>4</sub>-TCNQ molecules would be suppressed if the TCNQ molecules co-existed in the same position. These results show that dopant-blockade effect illustrated here remarkably suppresses the dopant diffusion and improve the stability of the DC-FET.

### **3.4. Conclusion**

In conclusion, I improved the device stability of the F<sub>4</sub>-TCNQ doped-contact PBTTT OFETs by adopting the dopant-blockade molecules (TCNQ). The dopant-blockade molecules were carefully selected to avoid the charge transfer reaction with the host materials, which was supported by the UV-Vis absorption spectroscopy. Furthermore, the selected dopant-blockade molecules were readily incorporated in PBTTT film by solid-state diffusion, investigated by elemental and structural analysis. By incorporating the dopant-blockade molecules, I demonstrated a more stable switching property of the doped-contact PBTTT OFET devices without affecting their electrical characteristics. The dopant-blockade molecules filled the dopant diffusion paths in PBTTT and effectively suppressed the diffusion of the dopant molecules. This study proposes a new strategy to enhance the stability of molecular doping methods in organic semiconductors, and reinforce the potential of OFETs by employing the contact doping techniques for resolving the contact resistance problem.

## References

- [1] L. V. Lingstedt, M. Ghittorelli, M. Brückner, J. Reinholz, N. I. Crăciun, F. Torricelli, V. Mailänder, P. Gkoupidenis, P. W. M. Blom, *Adv. Healthc. Mater.* **2019**, 8, 1900128.
- [2] D. J. Lipomi, Z. Bao, *MRS Bull.* **2017**, 42, 93.
- [3] W.-Y. Lee, H.-C. Wu, C. Lu, B. D. Naab, W.-C. Chen, Z. Bao, *Adv. Mater.* **2017**, 29, 1605166.
- [4] C. Kasparek, P. W. M. Blom, *Appl. Phys. Lett.* **2017**, 110, 023302.
- [5] T. Someya, Z. Bao, G. G. Malliaras, *Nature* **2016**, 540, 379.
- [6] H. Siringhaus, *Adv. Mater.* **2014**, 26, 1319.
- [7] M. Kaltenbrunner, T. Sekitani, J. Reeder, T. Yokota, K. Kuribara, T. Tokuhara, M. Drack, R. Schwödiauer, I. Graz, S. Bauer-Gogonea, S. Bauer, T. Someya, *Nature* **2013**, 499, 458.
- [8] H. Kang, R. Kitsomboonloha, J. Jang, V. Subramanian, *Adv. Mater.* **2012**, 24, 3065.
- [9] T. Sekitani, T. Someya, *Mater. Today* **2011**, 14, 398.
- [10] H. Yan, Z. Chen, Y. Zheng, C. Newman, J. R. Quinn, F. Dötz, M. Kastler, A. Facchetti, *Nature* **2009**, 457, 679.
- [11] V. Subramanian, P. C. Chang, J. B. Lee, S. E. Molesa, S. K. Volkman, *IEEE Trans. Compon. Packag. Technol.* **2005**, 28, 742.
- [12] A. R. Murphy, J. M. J. Fréchet, P. Chang, J. Lee, V. Subramanian, *J. Am. Chem. Soc.* **2004**, 126, 1596.
- [13] T. Sekitani, T. Someya, *MRS Bull.* **2012**, 37, 236.
- [14] L. Zhou, A. Wanga, S.-C. Wu, J. Sun, S. Park, T. N. Jackson, *Appl. Phys. Lett.* **2006**, 88, 083502.
- [15] A. Perinot, P. Kshirsagar, M. A. Malvindi, P. P. Pompa, R. Fiammengo, M. Caironi, *Sci. Rep.* **2016**, 6, 38941.
- [16] T. Uemura, T. Matsumoto, K. Miyake, M. Uno, S. Ohnishi, T. Kato, M. Katayama, S. Shinamura, M. Hamada, M.-J. Kang, K. Takimiya, C. Mitsui, T. Okamoto, J. Takeya, *Adv. Mater.* **2014**, 26, 2983.
- [17] F. Ante, D. Kälblein, T. Zaki, U. Zschieschang, K. Takimiya, M. Ikeda, T. Sekitani, T. Someya, J. N. Burghartz, K. Kern, H. Klauk, *Small* **2012**, 8, 73.

- [18] J. Youn, G. R. Dholakia, H. Huang, J. W. Hennek, A. Facchetti, T. J. Marks, *Adv. Funct. Mater.* **2012**, 22, 1856.
- [19] K. A. Singh, T. L. Nelson, J. A. Belot, T. M. Young, N. R. Dhumal, T. Kowalewski, R. D. McCullough, P. Nachimuthu, S. Thevuthasan, L. M. Porter, *ACS Appl. Mater. Interfaces* **2011**, 3, 2973.
- [20] Y.-Y. Noh, X. Cheng, M. Tello, M.-J. Lee, H. Sirringhaus, *Semicond. Sci. Technol.* **2011**, 26, 034003.
- [21] F. Gholamrezaie, K. Asadi, R. A. H. J. Kicken, B. M. W. Langeveld-Voss, D. M. de Leeuw, P. W. M. Blom, *Synth. Met.* **2011**, 161, 2226.
- [22] D. Boudinet, M. Benwadih, Y. Qi, S. Altazin, J.-M. Verilhac, M. Kroger, C. Serbutoviez, R. Gwoziecki, R. Coppard, G. Le Blevenec, A. Kahn, G. Horowitz, *Org. Electron.* **2010**, 11, 227.
- [23] X. Cheng, Y.-Y. Noh, J. Wang, M. Tello, J. Frisch, R.-P. Blum, A. Vollmer, J. P. Rabe, N. Koch, H. Sirringhaus, *Adv. Funct. Mater.* **2009**, 19, 2407.
- [24] P. Marmont, N. Battaglini, P. Lang, G. Horowitz, J. Hwang, A. Kahn, C. Amato, P. Calas, *Org. Electron.* **2008**, 9, 419.
- [25] D. He, J. Qiao, L. Zhang, J. Wang, T. Lan, J. Qian, Y. Li, Y. Shi, Y. Chai, W. Lan, L. K. Ono, Y. Qi, J.-B. Xu, W. Ji, X. Wang, *Sci. Adv.* **2017**, 3, e1701186.
- [26] C. G. Tang, M. C. Y. Ang, K.-K. Choo, V. Keerthi, J.-K. Tan, M. N. Syafiqah, T. Kugler, J. H. Burroughes, R.-Q. Png, L.-L. Chua, P. K. H. Ho, *Nature* **2016**, 539, 536.
- [27] S. Chung, M. Jang, S.-B. Ji, H. Im, N. Seong, J. Ha, S.-K. Kwon, Y.-H. Kim, H. Yang, Y. Hong, *Adv. Mater.* **2013**, 25, 4773.
- [28] T. Minari, P. Darmawan, C. Liu, Y. Li, Y. Xu, K. Tsukagoshi, *Appl. Phys. Lett.* **2012**, 100, 093303.
- [29] M. Kröger, S. Hamwi, J. Meyer, T. Riedl, W. Kowalsky, A. Kahn, *Appl. Phys. Lett.* **2009**, 95, 123301.
- [30] M. Kano, T. Minari, K. Tsukagoshi, *Appl. Phys. Lett.* **2009**, 94, 143304.
- [31] S. Cho, J. H. Seo, K. Lee, A. J. Heeger, *Adv. Funct. Mater.* **2009**, 19, 1459.
- [32] Y. Xu, H. Sun, W. Li, Y.-F. Lin, F. Balestra, G. Ghibaudo, Y.-Y. Noh, *Adv. Mater.* **2017**, 29, 1702729.
- [33] Y. Xu, H. Sun, E.-Y. Shin, Y.-F. Lin, W. Li, Y.-Y. Noh, *Adv. Mater.* **2016**, 28, 8531.

- [34] A. A. Günther, M. Sawatzki, P. Formánek, D. Kasemann, K. Leo, *Adv. Funct. Mater.* **2016**, 26, 768.
- [35] D. Khim, K.-J. Baeg, M. Caironi, C. Liu, Y. Xu, D.-Y. Kim, Y.-Y. Noh, *Adv. Funct. Mater.* **2014**, 24, 6252.
- [36] P. Reiser, F. S. Benneckendorf, M.-M. Barf, L. Müller, R. Bäuerle, S. Hillebrandt, S. Beck, R. Lovrincic, E. Mankel, J. Freudenberg, D. Jänsch, W. Kowalsky, A. Pucci, W. Jaegermann, U. H. F. Bunz, K. Müllen, *Chem. Mater.* **2019**, 31, 4213.
- [37] Y. Liu, M. D. Cole, Y. Jiang, P. Y. Kim, D. Nordlund, T. Emrick, T. P. Russell, *Adv. Mater.* **2018**, 30, 1705976.
- [38] F. A. Larrain, C. Fuentes-Hernandez, W.-F. Chou, V. A. Rodriguez-Toro, T.-Y. Huang, M. F. Toney, B. Kippelen, *Energy Environ. Sci.* **2018**, 11, 2216.
- [39] V. A. Kolesov, C. Fuentes-Hernandez, W.-F. Chou, N. Aizawa, F. A. Larrain, M. Wang, A. Perrotta, S. Choi, S. Graham, G. C. Bazan, T.-Q. Nguyen, S. R. Marder, B. Kippelen, *Nat. Mater.* **2017**, 16, 474.
- [40] J. Li, C. W. Rochester, I. E. Jacobs, S. Friedrich, P. Stroeve, M. Riede, A. J. Moulé, *ACS Appl. Mater. Interfaces* **2015**, 7, 28420.
- [41] A. Dai, A. Wan, C. Magee, Y. Zhang, S. Barlow, S. R. Marder, A. Kahn, *Org. Electron.* **2015**, 23, 151.
- [42] B. Lüssem, M. Riede, K. Leo, *Phys. Status Solidi A* **2013**, 210, 9.
- [43] I. Bruder, S. Watanabe, J. Qu, I. B. Müller, R. Kopecek, J. Hwang, J. Weis, N. Langer, *Org. Electron.* **2010**, 11, 589.
- [44] Y. Kim, S. Chung, K. Cho, D. Harkin, W.-T. Hwang, D. Yoo, J.-K. Kim, W. Lee, Y. Song, H. Ahn, Y. Hong, H. Sirringhaus, K. Kang, T. Lee, *Adv. Mater.* **2019**, 31, 1806697.
- [45] K. Kang, S. Watanabe, K. Broch, A. Sepe, A. Brown, I. Nasrallah, M. Nikolka, Z. Fei, M. Heeney, D. Matsumoto, K. Marumoto, H. Tanaka, S.-i. Kuroda, H. Sirringhaus, *Nat. Mater.* **2016**, 15, 896.
- [46] M. Nikolka, I. Nasrallah, B. Rose, M. K. Ravva, K. Broch, A. Sadhanala, D. Harkin, J. Charmet, M. Hurhangee, A. Brown, S. Illig, P. Too, J. Jongman, I. McCulloch, J.-L. Bredas, H. Sirringhaus, *Nat. Mater.* **2017**, 16, 356.

- [47] H. Méndez, G. Heimel, S. Winkler, J. Frisch, A. Opitz, K. Sauer, B. Wegner, M. Oehzelt, C. Röthel, S. Duhm, D. Többens, N. Koch, I. Salzmann, *Nat. Commun.* **2015**, 6, 8560.
- [48] S. Himmelberger, J. Dacuña, J. Rivnay, L. H. Jimison, T. McCarthy-Ward, M. Heeney, I. McCulloch, M. F. Toney, A. Salleo, *Adv. Funct. Mater.* **2013**, 23, 2091.
- [49] C. Wang, L. H. Jimison, L. Goris, I. McCulloch, M. Heeney, A. Ziegler, A. Salleo, *Adv. Mater.* **2010**, 22, 697.
- [50] T. Umeda, S. Tokito, D. Kumaki, *J. Appl. Phys.* **2007**, 101, 054517.
- [51] I. McCulloch, M. Heeney, C. Bailey, K. Genevicius, I. MacDonald, M. Shkunov, D. Sparrowe, S. Tierney, R. Wagner, W. Zhang, M. L. Chabinyc, R. J. Kline, M. D. McGehee, M. F. Toney, *Nat. Mater.* **2006**, 5, 328.
- [52] P. Reiser, L. Müller, V. Sivanesan, R. Lovrincic, S. Barlow, S. R. Marder, A. Pucci, W. Jaegermann, E. Mankel, S. Beck, *J. Phys. Chem. C* **2018**, 122, 14518.
- [53] J. Li, C. Koshnick, S. O. Diallo, S. Ackling, D. M. Huang, I. E. Jacobs, T. F. Harrelson, K. Hong, G. Zhang, J. Beckett, M. Mascal, A. J. Moulé, *Macromolecules* **2017**, 50, 5476.
- [54] C. Noël, S. Pescetelli, A. Agresti, A. Franquet, V. Spampinato, A. Felten, A. di Carlo, L. Houssiau, Y. Busby, *Materials* **2019**, 12, 726.
- [55] A. G. Shard, S. J. Spencer, S. A. Smith, R. Havelund, I. S. Gilmore, , *Int. J. Mass Spectrom.* **2015**, 377, 599.
- [56] F. M. Green, I. S. Gilmore, M. P. Seah, *Rapid Commun. Mass Spectrom.* **2008**, 22, 4178.
- [57] K. Kang, S. Schott, D. Venkateshvaran, K. Broch, G. Schweicher, D. Harkin, C. Jellett, C. B. Nielsen, I. McCulloch, H. Sirringhaus, *Mater. Today Phys.* **2019**, 8, 112.
- [58] S. N. Patel, A. M. Glauddell, K. A. Peterson, E. M. Thomas, K. A. O'Hara, E. Lim, M. L. Chabinyc, *Sci. Adv.* **2017**, 3, e1700434.
- [59] J. E. Cochran, M. J. N. Junk, A. M. Glauddell, P. L. Miller, J. S. Cowart, M. F. Toney, C. J. Hawker, B. F. Chmelka, M. L. Chabinyc, *Macromolecules* **2014**, 47, 6836.

## Chapter 4. Summary

In this dissertation, I described the research results mainly concerned with the electrical properties and operational stability of the doped-contact PBTTT OFETs. The main chapters were devoted to the material properties and electrical characterization of the doped-contact PBTTT OFETs with post-doping treatments including the surface etching, deposition of a passivation layer and the dopant-blockade method.

First, I demonstrated the enhancement of injection properties of PBTTT OFETs via solid-state diffusion, using the material combination of PBTTT and F<sub>4</sub>-TNCQ as the host and dopant materials, respectively, and a surface etching treatment by argon plasma was introduced for improving the devices stability. With the careful optimization of the deposition of the dopant molecules and etching process, the amount of neutral F<sub>4</sub>-TCNQ molecules on the PBTTT films was effectively controlled and the propagation of the doped regions into the active channel area of the PBTTT OFETs was significantly suppressed. Furthermore, the improvement of device stability by controlling the amount of dopant molecules via the etching process was not only identified by the experimental data of the trace of ON/OFF ratio of the doped-contact PBTTT OFETs, but also verified by a numerical simulation based on a modified Fick's diffusion equation that accounts for the capturing of diffusive neutral dopant molecules via charge-transfer. The band diagram analysis which was supported by low temperature measurement and UPS data of PBTTT films implied that the change of the dominant charge injection mechanism from thermionic emission to tunneling at the contact caused the improvement of charge injection properties after applying the contact doping. In addition, adopting Al<sub>2</sub>O<sub>3</sub> as a high-k gate dielectric material, I demonstrated the low-voltage operation organic transistors. For

these low-voltage operation devices, the doped-contact PBTTT OFET had a better performance compared to the pristine device.

Secondly, highly stable contact doping of the F<sub>4</sub>-TCNQ doped-contact PBTTT OFETs was achieved by incorporating TCNQ as the dopant-blockade molecule. The dopant-blockade molecule were carefully selected to meet two conditions; one was to avoid the charge transfer reaction with the host materials, and the other one was that the dopant-blockade molecule undergoes solid-state diffusion in PBTTT film. The investigation by UV-Vis absorption spectroscopy, elemental depth profiles and structural analysis revealed that TCNQ satisfied those conditions. Through incorporating the dopant-blockade molecules, the doped-contact PBTTT OFET devices exhibited a more stable switching property without affecting their electrical characteristics. TCNQ molecules blocked the dopant diffusion paths in PBTTT and effectively suppressed the diffusion of the dopant molecules.

This thesis provides a systematic pathway to utilize the doping technique by controlling the amount of dopant molecules and suppressing the dopant diffusion with dopant-blockade molecules. In addition, introducing a CYTOP encapsulation layer exhibited further improvement of stability. This study suggest that the molecular doping via solid-state diffusion is potentially one of the key techniques for resolving the contact resistance problem in OFETs.



국문초록

# 고체상태 확산 분자도핑에 의한 폴리싸이오펜계 유기 전계효과 트랜지스터의 전기적 특성 향상 연구

김영록

서울대학교 물리천문학부

유기반도체는 다른 반도체물질과 비교하여 소재의 유연성, 대면적 및 용액 공정의 장점을 갖고 있다. 이런 장점을 기반으로 유기반도체는 유기발광다이오드, 태양전지, 센서, 메모리 그리고 트랜지스터 등의 유기전자소자에 응용되고 있다. 이런 유기전자소자의 실질적인 응용을 위해 소자의 미세화 및 고속동작 소자의 구현이 필수적이다. 그러나 금속 전극과 유기반도체 사이의 쇼트키 콘택에 의해 발생하는 높은 콘택저항은 근본적으로 소자의 성능을 제한하게 된다. 실리콘 기반의 반도체 산업에서는 전극 주변의 반도체에 선택적인 이온주입 방법이 콘택특성을 향상시키기 위해 광범위하게 적용되고 있고, 이와 비슷한 접근법이 유기반도체에서의 콘택저항 문제를 해결하기 위해 응용될 수 있다. 최근에 여러 종류의 콘택도핑 방법론이 유기전자소자의 콘택저항을 감소시키기 위한 효과적인 기술로 보고된 바 있다. 하지만 소자의 스위칭 성능을 훼손하여 소자의 안정성을 두드러지게 악화시키는 도펀트 확산 문제로 인해 콘택도핑 방법론은 지금까지 유기 전계효과 트랜지스터에서 본격적으로 연구되지 않았다.

이런 측면에서, 본 학위논문에서 우선 바텀 게이트 구조의 폴리싸이오펜계 유기 전계효과 트랜지스터에 전하주입특성 향상을 위해 고체상태 확산에 의한 도펀트 분자( $F_4$ -TCNQ)의 선택적인 콘택도핑을 구현하였다. 소자의 구현 과정에서, 실험 결과와 확산방정식에 기반한 시뮬레이션을 활용하여 도핑 후 처리가 도펀트 분자의 확산에 미치는 영향에 관하여 연구하였다. 한편, 높은

유전율의 절연물질을 활용한 저전압 구동 유기트랜지스터에 분자도핑 기술을 적용하여 폴리머 도핑을 활용한 소자의 미세화와 저전력 유기소자의 가능성을 보여주었다.

한편 트랜지스터의 전극 영역에 도핑영역을 한정시키기 위한 도핑 후처리 도입에도 불구하고 도펀트 분자의 확산 문제는 완전히 해결될 수 없었다. 이 문제에 관하여, 도펀트 분자의 확산을 억제하기 위해 도펀트-차단 분자(TCNQ)를 폴리싸이오펜계 유기 전계효과 트랜지스터의 채널 영역에 선택적으로 주입하여 컨택도핑 방법론의 안정성을 향상시켰다. 이때 사용된 도펀트-차단 분자는 전기적으로 안정적이고 트랜지스터 채널 영역에서 도펀트 분자의 확산 영역에 자리 잡을 수 있는 분자를 사용하였다. 이 기술은 도펀트 분자 확산 영역을 도펀트-차단 분자로 채움으로써 도펀트 분자의 움직임에 대하여 효과적으로 장벽을 설치하는 것이었다. 이러한 도펀트-차단 방법론은 컨택저항 문제를 해결하는 유망한 방법론으로 컨택도핑을 도입하여 유기 전계효과 트랜지스터의 가능성을 극대화 하는데 기여 할 수 있을 것이다.

**Keywords:** 유기 전계효과 트랜지스터, 도펀트 분자, 컨택도핑, 고체상태 확산, 전하주입, 전하이동, 도펀트-차단

**Student Number:** 2016-30095

## 감사의 글

2014년 진로에 대한 고민을 가득 안고 대학원에 들어올 때 처음부터 다시 시작한다는 절박했던 마음이 떠오르며 이 글을 씁니다. 그 때는 지금의 지도교수님, 연구실 동료들과 6년을 함께 보내게 될 것이라고는 전혀 생각하지 못할 시기였습니다. 삶의 많은 기준을 다시 잡아가는 혼란스러운 시기에 친구들의 도움으로 지도교수님과 연구실을 결정할 수 있었습니다. 그리고 짧지 않았던 이 기간 동안 이렇게 많이 성장하게 될 것이라고는 기대하지 못할 때였습니다. 선물 같은 사람들이 제 주변에 없었더라면 이런 성장과 졸업이라는 기쁨은 느끼기 어려웠을 것입니다.

먼저 대학원 지도교수님이신 이택희 교수님께 감사의 말씀을 드립니다. 혼란스러운 마음과 친구들보다 늦게 대학원을 시작한다는 조금함으로 교수님을 찾아 뵈었는데 아무 조건 없이 흔쾌히 받아 주셨던 그때가 떠오릅니다. 6년이라는 긴 시간 동안 한 명의 연구자를 넘어 인격적으로 정말 많은 것을 교수님을 통해서 배웠습니다. 결과가 없어도 기다려주시고 지원해주시던 교수님 덕에 이 순간을 맞이 했습니다. 연구실을 나가서 때로는 도전의 시간을 만나더라도 교수님께서 보여주시던 기다림과 여유를 떠올리며 자랑스러운 제자가 되도록 노력하겠습니다.

학부 지도교수님이셨던 최선호 교수님도 잊을 수 없는 선생님입니다. 돌이켜보면 인간적으로 너무 부족한 저를 항상 크나큰 선의로 만나주셨던 최선호 교수님께도 감사 드립니다. 교수님의 그 너그러움으로 스스로를 돌아볼 기회를 만들 수 있었습니다. 많은 학생들이 존경하는 교수님으로 오랫동안 건강하게 지내셨으면 좋겠습니다.

함께 동고동락하며 연구실생활을 하던 동료들이 있어서 대학원생 시절이 즐거웠습니다. 먼저 머나먼 영국에서 박사를 마치고 기어코 서울로 온 기훈이. 기훈이가 아니었으면 정말 어떻게 졸업을 했을지 상상이 안될 꺼야. 문제를 끝까지 붙잡고 답을 찾는 치열함과 어떤 경우에도 친절할 여유를 갖는 기훈이에게 참 많은 것을 배웠어. 연구실에서 남은 시간 성과를 많이 거둬서 기훈이가 원하는 방향으로 진로가 풀리길 바라!! 학부 동기면서 대학원에 먼저 들어와 많은 것을 알려준 대경이. 때로는 연구를 공동으로 수행하면서 투닥투닥하던 시기도 있었는데 어느덧 옛 일이고 같이 졸업하는 구만. 앞으로도 종종 보자구~ 듬직한 우리연구실 랩장이자 오락대장 우철이. 우철아 내가 있어서 정말 든든하다. 우철이가 새로 시작하는 연구를 확실하게 이끌어줘서 가벼운 마음으로 졸업할 수 있는 거 같아. 어서 졸업해서 다시 동료로 만나자. 능력 있는 사회인에서 잠깐의 여유를 찾아오신 종훈 형님. 학교생활 충분히 즐기시고 우철이 잘 부탁 드립니다!! 여유 있는 팔자걸음 리치킴 준우. 연구가 수월하게 풀리지 않아 답답한 마음이 있을 건데 꾸준하게 노력하다 보면 반드시 결과를 얻는 거 같아. 너무 걱정하지 말아~ 유기팀 막내 희범이. 이미 1저자 논문이 있지만 요즘 들어 연구에 들이는 시간이 늘어나는 걸 보면 조만간 주도적으로 논문을 쓸 일이 있을 거 같아. 힘내!! 연구실 동기이자 우리 연구실 마스코트 2D팀장 갖재!! 재근이랑 그 힘들면서 또 보람찬 민홍기 교수님 수업 들은 것이 얼마 전 같은데..... 그 동안 거의 계속 옆자리 있던 재근이가 있어 즐거웠고 잘 챙겨줘서 정말 고마웠어. 하고 있는 연구 마무리 잘해서 좋은 논문 쓰길 바랄게!! 펍's 맘 지원이. 지원이가 들어온 것도 얼마 안된 거 같은데 벌써 이렇게 되었네. 우철이랑 즐겁게 연구하면서 좋은 연구도 많이 하고 무엇보다 좋은 소식 있길!! 전문연이 약이 된 재영이. 음악을 즐기며 항상 웃는 얼굴로 있어서 보기

좋았어. 가끔 놀리기도 했지만 형은 정말 재영이에게 좋~~~은 소식이 있으면 좋겠어 파이팅ㅋㅋ. 2D팀 막내 준태 본 날은 길지 않지만 지금처럼 주도적으로 연구실 생활 잘하고 재근이에게 많이 배우면 어렵지 않게 대학원 생활 마칠 수 있을 거야~ 우리 연구실 태양 왕택이. 만취한 모습도 전처럼 보이지 않고 연구열을 불태우는 모습을 보면 이제 끝이 멀지 않은 것 같아. 조금만 더 힘내자!! 같이 졸업하는 똑똑한 연식이. 우리 연구실 최연소 타이틀을 정말 오래 갖고 있었는데 시간이 정말 빠르다. 연식은 어디로 가든지 순발력 있게 잘 해낼 수 있을 거야~ 빠릿빠릿한 민우. 민우는 하는거 보면 예사롭지가 않아 암만 봐도 군필갈단 말이지 흠..... 지금처럼 빠릿빠릿하게 하면 군대문제도 잘 해결되고 졸업도 문제없이 할 수 있다고 믿어~ 분자팀 막내 중우 연구실의 미래를 부탁한다!!! 그리고 고은쌤 제가 이런저런 질문도 참 많이 드렸는데 항상 친절하게 답해주시고 그 동안 많이 챙겨주셔서 감사합니다~ 먼저 졸업하신 태영이형, 진곤이형, 영걸이형, 동구형, 현학이형 그리고 멧쟁이 경준이도 정말 감사했습니다!!

나의 대나무 숲 현우. 현우가 있어서 대학원 무사히 마치는 거 같아. 현우도 하는 연구가 있어서 마무리 돼서 졸업의 순간이 찾아오길 진심으로 바래. 대전에 내려가더니 올라오지 않는 천호. 나랑 천호는 정말 다른데 지향점은 비슷해서 참 잘 맞았던 것 같아. 같이 유럽여행 갔던 게 7년 전이라니..... 앞으로도 잘 부탁해!! 그리고 거의 매일 보며 운동을 함께해온 인석이형. 졸업 이후에도 학교에 남아서 같이 운동해서 즐거웠어. 조만간 교수로 자리 잡아서 거 하게 밥 한번 살 그날을 기다릴게!!! 잘하면 재미있다는 말로 먼저 회사에 보내버린 무송이. 자신감 있는 모습이 참 보기 좋았어 이제는 다시 한술밥 먹는데 재미있게 지내ㅎㅎ 대학원 룸메이트 창현이도 졸업이 얼마 안 남았는데 즐거운 시간 보내길 바래요!! 지금은 미국에 유학 가있는 통계대학원생 민성이. 미국병 완치하고 유학생활 잘 마치길 기원할게!! 월요모임을 함께했던 진영곰, 재준이형, 경석이형, 창휘, 동현 그리고 이전에 졸업한 사람들 정말 즐거웠어~

인간적인 성장에 많은 영감과 기회를 준 큰은혜교회 친구들에게도 감사의 말을 전합니다. 챙겨주시고 성장의 자극을 주셨던 지선 누님. 가끔 도라에몽 성대모사를 하며 처음되는 길을 걷고 있는 상희. 생각이 깊고 중심이 명확한 승기. 그리고 학위를 마무리하는 시기에 저와 함께 하며 기쁨을 나누고 인간적인 성장에 많은 자극을 주었던 유정이에게 감사의 말을 전합니다.

끝으로 때로는 갈지자로 나아가는 아들의 선택을 묵묵히 바라보며 응원하고 기도해주는 부모님. 저를 생각하면 항상 안타까워하시는 것 같지만 전 제 선택에 만족하고 충분히 행복한 삶을 살고 있다고 믿어요. 지금까지 애쓰고 마음 써주셔서 고마워요. 앞으로의 삶도 지켜봐 주시면 좋겠어요~ 그리고 형이 집에 많이 신경 쓰지 못하는데 마음 씩씩이가 섬세한 동생 영빈이가 집에 있어줘서 고마웠어.

이외에도 제가 도움을 받은 분들이 정말 많은데 이름을 다 적지 못해서 죄송하고 또 감사드립니다. 뒤돌아 보면 보이지 않는 수많은 기적이 쌓여 지금이 있음을 느낍니다. 언제나 겸손하고 감사하는 사람이 되기를 다짐하며 먼저 도움의 손길을 건네는 삶을 살도록 노력하겠습니다. 학교를 떠나 새 길을 나서야 하는 때에 지금까지 그랬던 것처럼 앞으로도 주님께서 제 걸음을 인도하시기를 기도하며 이 글을 마칩니다. 감사합니다.